

Characterization of the Influence of Thermal Profile on Microstructural Development in a Eutectic Cobalt Silicon Alloy

Submitted By
Andre V. Cleaver

IN PARTIAL FULFILLMENT OF THE REQUIREMENTS FOR THE DEGREE OF
MASTER OF SCIENCE IN MECHANICAL ENGINEERING

School of Engineering
Tufts University
Medford, Massachusetts

May 2018

Signature of Author:
Andre V. Cleaver

Certified By:
Associate Professor Douglas M. Matson
Department of Mechanical Engineering
Tufts University

Committee:
Associate Professor Luisa Chiesa
Department of Mechanical Engineering
Tufts University

Committee:
Assistant Professor Darryl Williams
Dept. of Chemical & Biological Engineering
Tufts University

Abstract

The purpose of this study is to develop a new image processing technique to evaluate decanted structures of undercooled alloys. Dendrite growth theory reveal a trend of decreasing dendrite radii as undercooling levels increases, and a similar decreasing trend with increasing convection rates at lower undercoolings. Experiments were performed to evaluate if optical microscopy could be used to quantify decanted surface structures following rapid solidification of eutectic CoSi₆₂ at% alloys. Dendrite diameters decrease with increasing undercooling except for tests conducted with applied stirring at low undercoolings. The higher the convection, the greater the deviation. Marangoni stirring was induced by irradiating a small target area on the surface of levitated molten samples. For a 0.5W laser input the characteristic diameter was half the unstirred value. For 2.4 W laser input this factor drops to one third. The developed imaging technique was able to produce these trends when identifying the primary phases.

Acknowledgements

The author wishes to acknowledge partial financial support for this work provided by NASA under the “ELFSTONE” grant NNX16AB59G. Special thanks to the NASA Marshall Space Flight Center Electrostatic Levitator team including Michael SanSoucie, Trudy Allen, and Glenn Fountain and Tufts University Postdoctoral Fellows Sangho Jeon, Xiao Xiao, and Gabrielle String. I would also like to thank my thesis committee Dr. Douglas Matson, Dr. Luisa Chiesa, and Dr. Darryl Williams for their guidance and support.

Table of Contents

1	Introduction	1
2	Background	4
2.1	Nucleation	4
2.2	Containerless	5
2.3	Marangoni Effect	6
2.4	Undercooling	6
2.5	Recalescence	7
2.6	Dendrite Growth Theory	11
2.7	CoSi Model System	12
2.8	Previous Literature	13
3	Experimental Procedure	16
3.1	Data collection	16
3.2	Sample Preparation	16
3.3	Electrostatic Levitation	17
3.4	Laser System	18
3.5	Pyrometer	18
3.6	Pyrometer Correction	18
3.7	Calibration	20
3.8	Image Processing	26
3.9	Data Analysis	30
4	Results	38
5	Discussion	44
6	Conclusions	47
7	Future Work	49
8	References	51

List of Tables

Table I	Thermophysical Properties of CoSi and CoSi ₂	31
---------	---	----

List of Figures

Figure 1	Phase diagram of Cobalt Silicon	3
Figure 2	Marangoni Convection Effect	6
Figure 3	Double Recalescence of an CoSi ₆₂ alloy	9
Figure 4	CoSi and CoSi ₂ as a function of undercooling	14
Figure 5	Schematic of the ESL system at NASA/MSFC	17
Figure 6	Positioning of Levitated Samples	21
Figure 7	Burn Test	22
Figure 8	Power curve of the YAG laser	23
Figure 9	Plot of Temperature and Voltage as a function of time	26
Figure 10	Phenom Pro-X SEM	27
Figure 11	Back-scattering SEM images	28
Figure 12	A partial processed SEM image	28
Figure 13	Vision Assistant	29
Figure 14	Recalescence temperatures due to shift in composition	32
Figure 15	Phase Diagram of Primary CoSi	33
Figure 16	Phase Diagram of Primary CoSi ₂	34
Figure 17	Pixel Intensity for Identified Dendrite Head	36
Figure 18	Circle detection function in Vision Assistant	37
Figure 19	Plot of Average Dendrite Radii CoSi	38
Figure 20	Plot of Average Dendrite Radii CoSi ₂	39
Figure 21	Plot of average % area CoSi	40
Figure 22	Plot of average % area CoSi ₂	41
Figure 23	Distribution of # of Radii (1/4)	41
Figure 24	Distribution of # of Radii (2/4)	42
Figure 25	Distribution of # of Radii (3/4)	42
Figure 26	Distribution of # of Radii (4/4)	43

Nomenclature

A	Surface Area [m^2]
C_p	Specific Heat [$\frac{J}{mol}K$]
ε	Emissivity
f_s	Fraction solid by mole
H_f	Heat of Fusion [J/mol]
$\frac{dT}{dt}$	Heat Transfer rate [K/s]
λ	wavelength [nm]
m	Mass [mol]
w_o	Mole Concentration of Si in Eutectic alloy
w_l	Mole Concentration of Si in remaining melt
w_s	Mole Concentration of Si of in Primary phase
q_{las}	Heat Energy provided by laser [J/s]
q_{rad}	Heat Loss by Radiation [J/s]
I	Radiance by Planck's Law [$W \cdot sr^{-1} \cdot m^{-2}$]
R	Approximated dendrite tip radii [m]
γ	Surface Tension [N/m]
σ	Stefan-Boltzmann Constant [WmK^{-4}]
ΔT	Thermal Undercooling [K]
T	Temperature [K]
T_{env}	Temperature of Environment [K]
TR1	Primary Recalescence [K]
TR1 [^]	Corrected Primary Recalescence [K]
$\Delta TR1$	Undercooling of Primary Recalescence [K]
TR2	Secondary Recalescence [K]
$\Delta TR2$	Undercooling of Secondary Recalescence [K]
Δt	Delay-time [s]

1 Introduction

The purpose of this study is to develop a new image processing technique to evaluate decanted structures of undercooled alloys. Currently, no technique exists to quantify the surface area of selective phases following solidification. The development of this imaging technique will provide insights into developing dendrites such as volume and decanting behavior. A binary alloy with large partition between its respective terminal eutectic phases makes an ideal selection for this study to show clear changes in grain sizes as a function of processing parameters upon visual inspection.

Many processing parameters and their role in microstructure development have been study in detailed. These include growth velocity, melt convection, undercooling, and heat transfer rates in common alloy model systems [1]. Large partitioning which occurs during rapid solidification is believed to hinder the growth velocity of the first dendrite structures. Because of the nature of solute rejection that occurs between the dendrite and the liquidous region, convection rate is selected as the changing parameter for this study. Fluid flow effects on the solute particles potentially relieves the burden the dendrites face in the primary recalescence.

Control of laminar convection is essential for this study, for turbulent convection rates fragment primary dendrites in the metastable phases [2]. Thus, this study utilized the Electrostatic Levitator (ESL) at NASA-Marshal Space Flight Center (MSFC) as greater laminar convection rates can be controlled with heating power which takes advantage of the Marangoni Effect in spherical samples. Jeon and Matson utilized the ESL at NASA-MSFC to test CoSi alloys of the same compositions. The molten samples freely cooled to the surrounding environment set at 300 K through

radiation. The approach I will use will be similar to this methodology in [3]. The exception is I will continue lower level heating at different power settings during the cooling phase to continue convectional effects. By continuously heating the system, the Marangoni Effect will continue as convection is shown to be proportional to the temperature difference and hence the energy input. In addition, I will apply this laser treatment to a wide range of undercooled values to gain insights to fluid flow velocity and dendrite growth velocity in relation to the thermodynamic driving force.

The most common method to examine the microstructure of metallic alloys is the scanning electron microscope (SEM) [4]; however, only internal structures have been observed and they cannot provide quantitative information such as volume and fraction solid formed due to the uncertain direction of the cross sectional slices. Surface SEM images display grayscale (pixel intensities 0-255) images, making them compatible for image processing functions to discriminate regions such as voids, primary structures, and residual liquidous melts that remain between close dendrite arms.

For this study, optical microscopy was used to quantify decanted structures following rapid solidification of eutectic Cobalt Silicon (62 at.% Si) (CoSi62) alloys. Figure 1 shows the phase diagram of Cobalt Silicon. This model system is selected due to the large partitioning at the eutectic composition, making this alloy attractive for this convection study.

The development of an image processing technique to numerically characterize the geometric structures may provide insights into the decanting behavior and grain size control for other binary alloy systems.

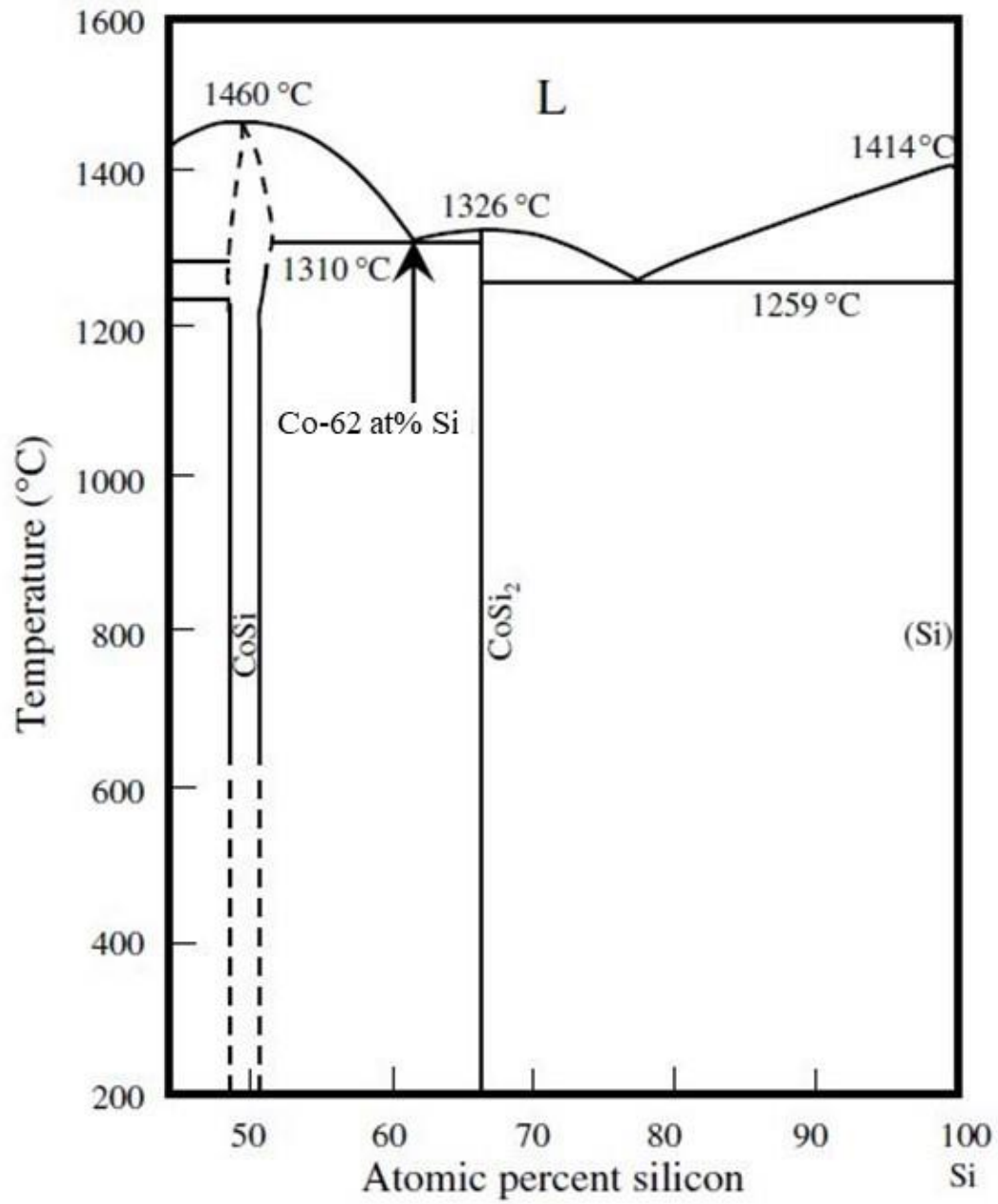


Figure 1. Phase diagram of Cobalt Silicon. Eutectic terminal compositions of CoSi₆₂ are (CoSi 50 at% Si) and CoSi₂ 66.67 at% Si) [2].

2 Background

Many casting methods yield different microstructures upon examining both the interior and exterior surfaces due to the numerous nucleation points during solidification. These nucleation points can come from either internal contaminants such as oxides or contact by a container [5, 6]. Eliminating contaminants is difficult to achieve but is at best carried out by superheating the samples for short periods. Eliminating the contact between a molten sample and a container significantly reduces potential nucleation sites. Numerous containerless processing methods can be utilized with Electrostatic (ESL) and Electromagnetic levitation (EML) being the most common techniques.

Nucleation

Solidification for any material begins from a cluster of molecules in the liquid that bond together to form a nucleus or nucleus point. If a nucleus forms when provided with a sufficient amount of particles of the material a homogeneous nucleation occurs. The nucleus point serves as the origin for the crystal to grow. The size of the individual crystals depend on the number of nucleation points, and they could continue to grow until the crystals collide into one another. The roughness of any container provides heterogenous nucleation. This type of nucleation is more common as compared to homogenous nucleation and begins on foreign surfaces or particles such as oxides. [7, 8]

Containerless Processing

Studying the thermophysical properties of metallic samples are best conducted in the samples' liquid state [9-14]. In this study, we utilized Electrostatic Levitation (ESL) as opposed to the Electromagnetic Levitator (EML).

EML utilizes high frequency currents that generate a magnetic field which levitates samples of moderately sized samples ($d \sim 6$ mm) and testing may be accomplished in vacuum or in an inert gas environment. Internally, eddy currents are formed which also generates an opposing magnetic field. On ground, it is possible to overcome the force of gravity if the opposing magnetic fields from both the sample and the coils of the EML are properly designed [15, 16]. The disadvantage is the amount of current that must be supplied to levitate the sample on ground. Overcoming gravity to levitate samples requires lots of power, but it also causes the internal circulation to reach turbulent flows. Therefore, laminar flow is unachievable. This issue is addressed in space due to a microgravity environment; however, this approach costs greatly.

The ESL facility is composed of two oppositely charged horizontal plates with the sample placed between them. An electric field is generated which charges and suspends a sample in a relatively constant fixed position. Testing is done in vacuum to limit discharge arcing. Sample sizes are smaller (approximately $d \sim 2$ mm) because the electric field generated by the ESL can overcome the force of gravity on the sample to an extent. Larger samples would require a stronger electric field but will produce an arc [8]. A disadvantage is that samples of small sizes are susceptible to evaporation losses once above melting temperatures. The main advantage to ESL is a more quiescent sample flow condition in ground testing compared to ground EML.

Marangoni Effect

The Marangoni effect refers to fluid flow due to surface motion induced by a temperature gradient causing surface tension changes. In this study, samples are exposed to one-sided heating creating a hot side and a cooler side. The gradient in temperature creates a low and high surface tension respectively. The difference in surface tension within the spherical sample will then cause motion and an internal circulation flow as depicted in Figure 2 will be initiated [17-19].

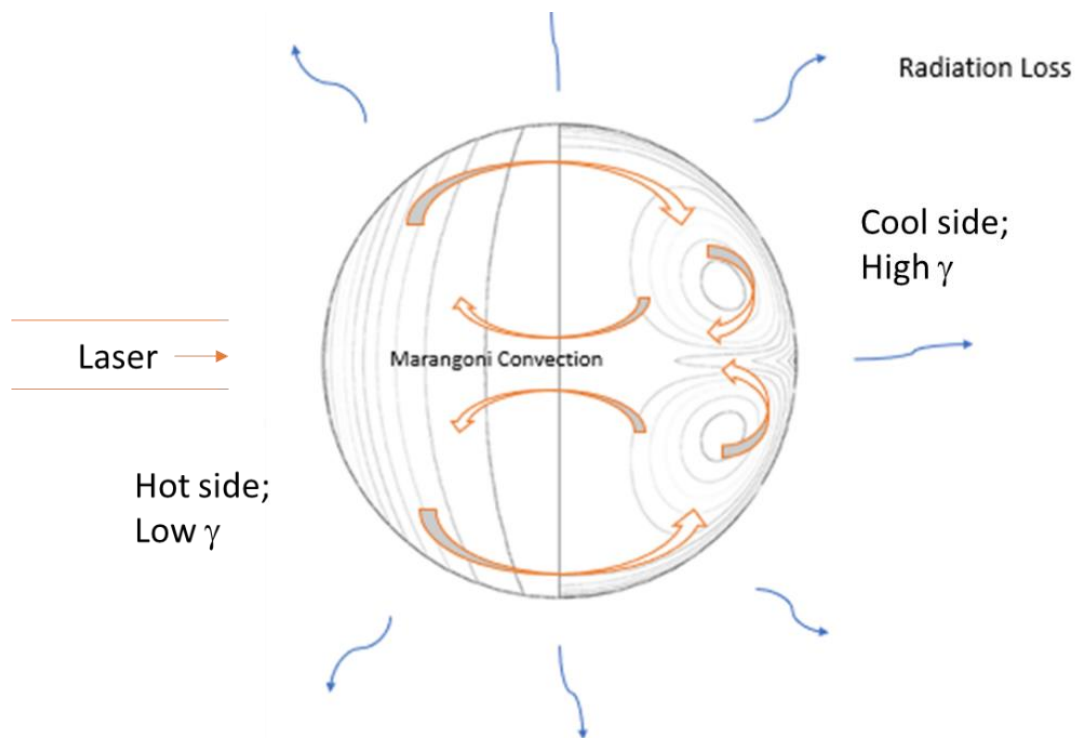


Figure 2. Illustration of the Marangoni Effect created by one-sided heating.

Undercooling

As mentioned earlier, the process for solidification requires a nucleation site as a material's temperature decreases to its solidification point. In the case where no

nucleation point is present, the material can continue to exist in its liquid phase. This process is called undercooling [3].

Recalescence

Recalescence is an event in which a cooling sample reheats to its equilibrium state. Double recalescence is an event in which the sample will reach its equilibrium point in two steps. The first step involves conversion from liquid to metastable phase and the second involves formation of the stable phase. For Cobalt Silicon alloys used in this study the undercooling determines which phase forms first and which forms second. The two phases involved are CoSi_2 with a fluorite (CaF_2) structure and equiatomic CoSi with a simple cubic (FeSi) structure. In either case, the second phase grows around and within the primary structure [20].

For metals/alloys to experience rapid solidification, they must undercool. And for solidification to occur, there must be a nucleation point as a starting position. In the case of containerless processing, the nucleation point is often a contaminant such as an oxide particle.

Recalescence occurs resulting in rearrangement of atoms to the lowest energy state [21]. The energy removed from the newly formed solid is transferred into the liquidous region which can be recognized as the spike in temperature during the cooling stage. Figure 3 shows an example of a thermal profile for a CoSi sample that completed a full melt cycle. This melt cycle is partially outlined in the appendix B. Two recalescence can be seen; the black line represents the raw data. The slight oscillations are due to the Pyrometer laser reading the oxides as the sample is rotating wildly. The true temperature reading is accepted as the lowest portion of the

oscillations. Graphing software OriginPro 8.5 applied the envelope function which generated a plot interpolation of the lowest value points which can be seen in red. The envelop function is a curve that is tangent to every peak in the source dataset. This function works by finding all the points whose first-order derivative is equal to zero. A cubic spline interpolation is performed for these points and the “smoothing” action is dependent on a user input value for adjacent-averaging. This type of averaging takes the average of number of a certain number of data points (user input) around each point in the original data.

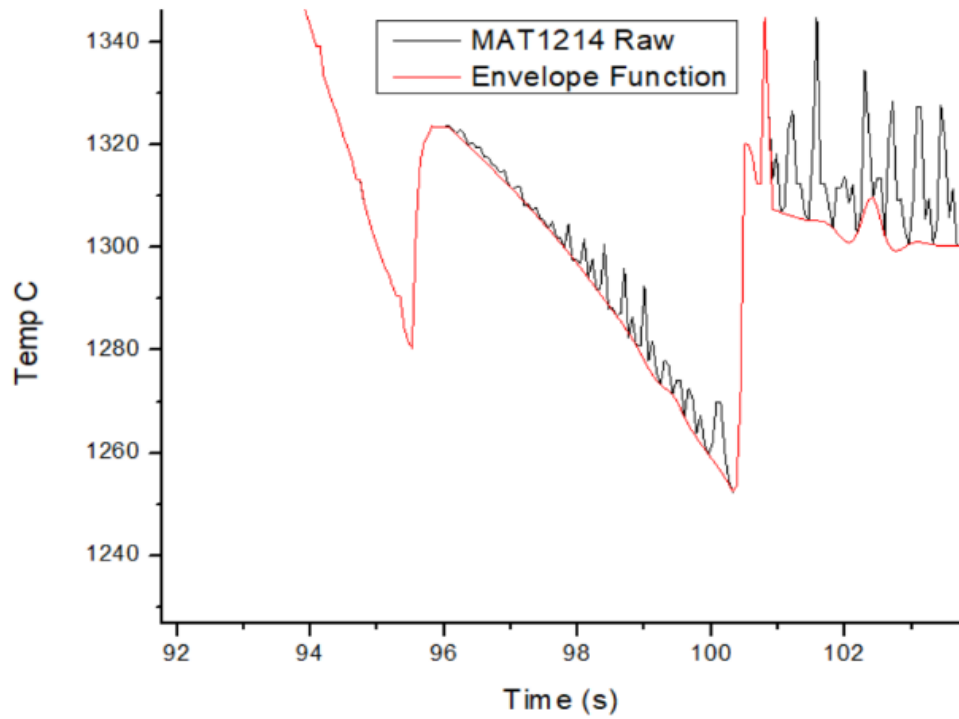
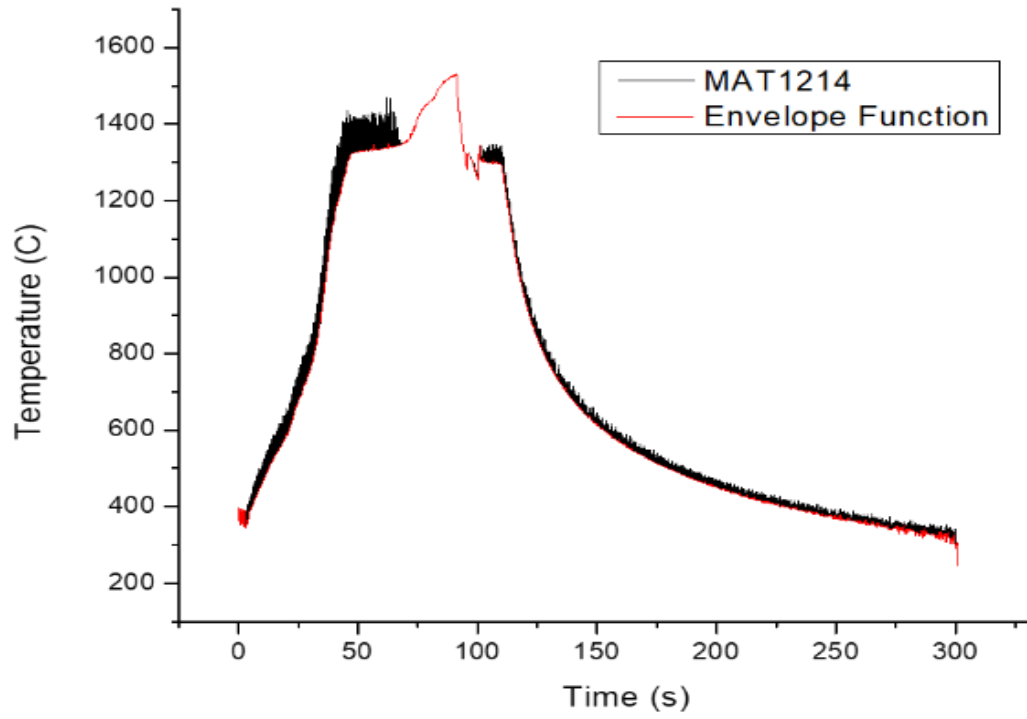


Figure 3. Double Recalescence of an CoSi_6 alloy. (top) shows a full thermal cycle and (bottom) is a zoomed-in picture of the double recalescence event. The two sharp

spikes in temperature indicates a thermal event. The delay time between the two events is ($\Delta t \sim 4$ seconds as seen on the figure on the right).

The delay-time is the time between each recalescence events and can be influenced by convection rates [2].

This study is interested in the undercooling of the first recalescence (TR1) event. TR1 corresponds to the first dendrite structures to form in rapid solidification. Physically, the molten samples first undercools. The sample then recalesces due to nucleation sites (some contaminant) and forms the metastable phase. Several studies have explored the crystallization pathway and growth mechanisms that stem from the metastable phase or “mushy-zone” [22-25]. The sample continues to undercool and the remaining melt decants, or pulls away, from the surface due to solidification shrinkage. The density of the liquid is greater than the solid that is forming and thus with solidification if the outer shell is hard, the internal regions pull fluid back leaving decanted solid protruding from the surface. The level of decanting depends on the level of undercooling until the 2nd recalescence event occurs. Coarsening and re-melting of the stable phase begins as the second phase grows in and around the primary dendrites. Depending on the degree of undercooling, generally lower (ΔT) will form CoSi in the primary structures followed by CoSi₂ in the second recalescence. The reverse is observed for greater ($\Delta T \sim > 90$ K) [2, 3, 26, 27]. Any level of undercooling demonstrates competitive nucleation and the growth kinetics of the two step phases [20, 25, 28, 29]. Further into greater ΔT values, the microstructures display evidence of decanting when the remaining melt continues to cool after the primary recalescence. The remaining liquid melt contracts and is pulled to the center of the sample leaving

behind solid phase. This decanting of fluid is similar to the exposure of submerged rocks as the tide goes out on a beach. The exposed dendrite structure is thus frozen in time with subsequent microstructural evolution prevented. This study relies on this process of freezing-in of transient microstructures to gain evidence of how structural evolution takes place during solidification.

Dendrite Growth Theory

LKT Theory

The Lipton-Kurz-Trivedi or LKT Theory relates dendrite growth velocity to the depth of undercooling and minimum radius of the dendrite tip [30]. Primary and secondary dendrites are both influenced by the degree of undercooling. Growing dendrites must reject heat into the neighboring phases during solidification. Thus, heat capacitance (C_p) of the liquid and metastable phases, with the latter having a greater value, are important. In the primary recalescence, the metastable phase is first formed, and the dendrites continue to reject heat as it grows through liquid. In secondary recalescence, the stable dendrites run into the issue of the metastable phase having a greater C_p which must re-melt in order for the dendrites to grow. [30-34]

Theoretical Tip radius

The radii of the primary dendrite heads are mainly influenced by the growth velocity which has a positive correlation to the degree of undercooling. Generally, the deeper the undercooling, the greater the thermodynamic driving force and thus velocity the dendrites have in growing within the phases. According to theory, the radii of the

primary dendrite heads decreases as the growth velocities increases [28, 29, 35-37].

Directional growth of the dendrites were explored in [38, 39] and diffusion transport in [40].

Partitioning

Solute rejection occurs at the interface between the liquid and metastable phase during the dendrite growth. With the solute rejection also occurring normal to the dendrite tip, the presence of solute atoms may act as obstacles to the growing dendrite. These atoms form a phase which may have a heat capacitance greater than the surrounding liquid which influences how the dendrites distribute and reject heat within the liquid. [41, 42]

Limitations

The LKT theory is valid only for diluted structures and CoSi₆₂ alloy system violates this condition, and therefore, this theory cannot be applied to this study. However, this study considers the general trend of decreasing radii with increasing undercoolings.

Cobalt-Silicon Model System

CoSi₆₂ is selected for multiple reasons. First, the eutectic CoSi₆₂ represents a model system [43-45]. It has two known terminal phases CoSi and CoSi₂; therefore, no other metastable reaction can occur. The Silicon composition for the terminal phases are 50% and 66.7% respectively which are necessary in calculating shifts changes in

composition after thermal events. This large difference in composition results in enormous partitioning of rejected solute particles in the developing dendrites in primary phase. As mentioned earlier, these particles potentially serve as road blocks in the path of the dendrites and thus reduce the growth velocity. Following the general trend of the LKT theory, the reduced velocity which is proportionally related to low undercoolings result in larger dendrite tip radii.

Second, CoSi₆₂ specifically has been investigated by research groups who are also interested in microstructural development. This study may provide insights to additional preparation steps for the processing of the alloy system to improve material properties.

Previous Literature

This study stems from the work performed by Jeon and Matson [3] who explored various degrees of undercooling and delay-time of CoSi₆₂ and reports the relationship between emissivity, delay-time, and surface growth. This study found emissivity to be a unique parameter that changes with the delay-time and becomes a function of surface area. An additional note is the crossover between the competitive phases as a function of undercooling. In Figure 4, Jeon and Matson [3] determined a general amount of undercooling is approximately ($\Delta T \sim 100$ K) for the formation of CoSi₂ in the primary phase based on the work of Li and Zhang [2, 26]. Here the delay time between phases is plotted against undercooling. Undercoolings below 100 K shows the delay time for the formation of CoSi. As the undercooling increases the delay time decreases. The same goes for undercoolings greater than 100 K for the

formation of CoSi_2 . This trend is common for other metallic systems. At the transition point ($\Delta T \sim 100 \text{ K}$), both phases CoSi and CoSi_2 grow at the same time resulting in a delay time.

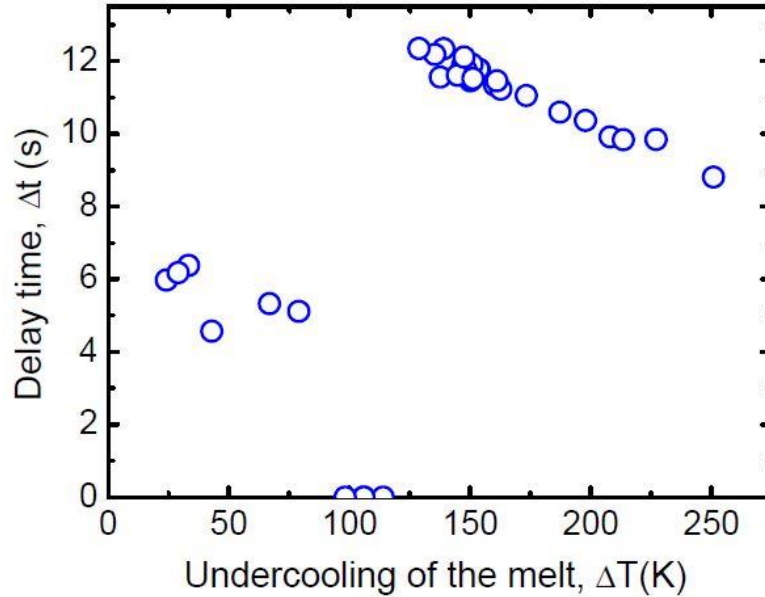


Figure 4. Plot of changes in delay time that corresponds to CoSi and CoSi_2 as a function of undercooling. Here, the approximate undercooling limit to determine primary phase is ($\Delta T \sim 100 \text{ K}$) [3].

The work performed by Mingjun [2] examined the solidification pathway of CoSi -61.8 at. % in both EML and ESL with X-ray synchrotron as a tool to confirm the phases at given undercooling values. This work determined that phase competition between CoSi and CoSi_2 is dependent on undercooling ($\Delta T \sim 88 \text{ K}$) which focuses in on a nucleation barrier. This conclusion was determined not the case in Jeon and Matson [3]. The work conducted by Yao [27] reports two eutectic compositions of CoSi - 62.1 & 43.5 at % and relate the diameter size to unique microstructure in drop tube testing. Zhang [26]

examined the solidification of CoSi-61.8 at. % using multiple containerless facilities (e.g. EML, ESL, and glass-fluxing) and determined that melt convection has no effect on the primary phase selection in undercooled melts. ESL processing creates laminar flows compared to the alternative EML processing in which turbulent flow exists. These violent convection rates breakdown the stable dendrite structures. Mingjun [2] concluded that the fluid flow generated in ESL is insignificant as the dendrite structures remain intact and continued to grow into the neighboring region. For this study, the dendrite structures must remain intact to evaluate the changes in grain size; therefore, ESL processing can only be used.

3 Experimental Procedure

Data Collection

It is common to measure properties of metals and metallic alloys in their liquid state. These properties are used to predict convection behavior in casting procedures. Containerless processing is effective in measuring a molten metal's thermophysical properties as the removal of physical nucleation sites allows access to metastable phases and deep undercoolings. This experiment required an ESL facility as the question of increasing convective stirring is the dataset of interest.

Sample Preparation

Both Cobalt and Silicon were purchased from *Alfa Aesar* Haverhill, MA, USA (Co 99.95%, Si 99.999%). Pre-processed CoSi62% eutectic samples were prepared at the Solidification Laboratory at Tufts University. Calculated amounts of Silicon and Cobalt were filed/cut and weighed to match the desired CoSi62at% composition using a Mettler Toledo Scale AX105 (± 0.03 mg). The samples were then arc-melted under an Ar atmosphere at NASA-MSFC. Samples are weighed post-arc to ensure no significant mass change during the arc-melting process. Any sample with greater than 2% mass change were discarded from the study because the sample composition is no longer known. Additional samples of the same composition were prepared to increase the sample size; however, the arc-melting process took place at Tuft's Solidification lab. A total of 20 samples were prepared that ranged from (30-45 mg) and were approximately (2 mm) in diameter.

Electrostatic Levitation Facility

The NASA facility at the Marshall Space Flight Center operates the Electrostatic Levitator in a vacuum chamber (4.7×10^{-7} Torr). Two electrodes generate an electrostatic field with an input voltage (10 kV nominal, 15 kV maximum) which charges and suspends the samples [8]. A Pyrometer (Mikron MI-GA140 single-color $1.45 - 1.80 \mu\text{m}$ wavelength) and a Phantom high-speed camera were used to record and capture the thermal profiles and solidification process. A schematic of the ESL system is shown in Figure 5.

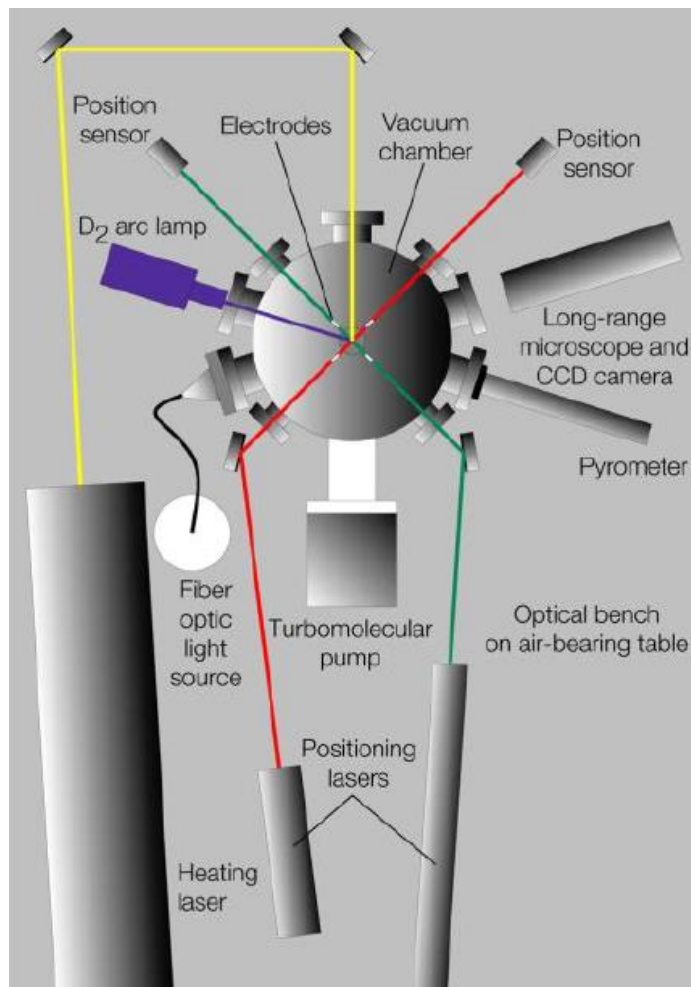


Figure 5. Schematic of the ESL system at NASA/MSFC [7, 8]

Laser System

Besides melting the CoSi alloys, this study must also reduce the energy input instantly at consistent levels. To control this energy transfer, a heating laser is the ideal tool to utilize and the power output is manually controlled by a corresponding voltage setting. A power curve as a function of voltage can be gathered from the laser's operating manual. The laser system of the ESL facility utilizes a 200W YAG laser meaning the material used to concentrate the light energy is a crystal specifically, neodymium-doped yttrium aluminum garnet; Nd:Y₃Al₅O₁₂. To melt the CoSi alloys in a sealed chamber a heating laser This laser allows for fine

Pyrometer

Measurement of the samples were carried out with a Radiation Pyrometer MIKRON MI-GA140 which operates with a single spectral range single-color 1.45 - 1.80 μm. A radiation pyrometer is used for this study because the sample of interest remains in sealed chamber. In addition, the samples reach temperatures at 1587 K and must be measured without any physical contact. The emitted irradiation from the sample provides a method to acquire the temperature, and thus, radiation pyrometer is the ideal tool to gather the temperature profile.

Pyrometer Correction

Changes to the transmissivity of the optical path or slight variation in surface condition (oxides or surface roughness) result in a reading of the liquidus temperature which may not exactly agree with published values. To correct this error one-color

radiation pyrometer theory was applied. This theory eliminates emissivity by declaring ratios until certain assumptions hold true as explained to follow. At a specific wavelength, the intensity of radiation I , can be calculated with Wein's approximation to Planck's radiation equation (1) with known constants $C_1 = 3.742E8 \text{ W} \cdot \mu\text{m}^4/\text{m}^2$, $C_2 = 1.439E4 \mu\text{m} \cdot \text{K}$

$$I = \frac{C_1}{\lambda^5 [\exp\left(\frac{C_2}{\lambda T_b}\right) - 1]} \quad (1)$$

where T_b is the apparent temperature of a black body working at a wavelength λ . With the equation (2) for a Black Body:

$$\left(\frac{1}{T} - \frac{1}{T_b}\right) = \frac{\lambda}{C_2} \varepsilon_\lambda \quad (2)$$

where $\left(\frac{1}{T} - \frac{1}{T_b}\right)$ is the error in a pyrometer measurement to a reference temperature. For a given signal at a given reference temperature and emissivity, a second observed signal will correspond to a predicted new temperature T_L . Any pyrometer has a pre-programmed value of emissivity and T_L . By taking the ratio of the intensities followed by the natural logarithm the equation (3) simplifies to:

$$\ln\left(\frac{I}{I_0}\right) = -\frac{C_2}{\lambda} \left(\frac{1}{T} - \frac{1}{T_0}\right) \quad (3)$$

The ratio remains constant using whether you are using the pre-programmed temperature conversion basis or the new reference temperature basis. Therefore, the ratio of intensities at the liquidus temperature and the pyrometer reading becomes (4):

$$\ln\left(\frac{I}{I_L}\right) = \ln\left(\frac{I_P}{I_{PL}}\right) \quad (4)$$

Thus the resulting equation becomes:

$$\frac{1}{T} = \frac{1}{T_p} + \left(\frac{1}{T_L} - \frac{1}{T_{PL}}\right) \quad (5)$$

Where T_L is the reference liquidous temperature of CoSi (1578 K), T_{LP} is the melting temperature observed by the pyrometer, T_P is the temperature reading from the pyrometer, and T is the corrected temperature. This temperature is called the radiance method.

Calibration

The first calibration that was performed was the melt processing of a pure Zirconium (Zr) sample with known thermal properties to ensure the accuracy and precision of pyrometer readings. The peak temperature readings revealed the center point of the laser target position. The laser is corrected in both X (yaw) and Y (pitch) directions to strike the center of the levitated target sample. Once the center has been determined, the device controlling the laser position is turned off thus locking the position. Due to the location of the ESL facility viewing ports, the video recorder and heating laser target are on the same equatorial plane but are oriented 20 degrees from each other. To address this issue, a digital grid was applied to the monitor that displays a live image of the sample. These grid lines can be manually shifted to box any region of interest. A digital grid was applied to the Zr sample while levitated to ensure

the positioning of samples were consistent while exposed to the electrical field. Subsequently, the CoSi62 samples were levitated and observed to remain in the digital box throughout the experiment. Image processing will later be used to determine the center point of samples remained within the center of the box ensuring proper laser targeting at the desired center point. Figure 6 shows four levitated samples of different mass that each remain within the digital box.

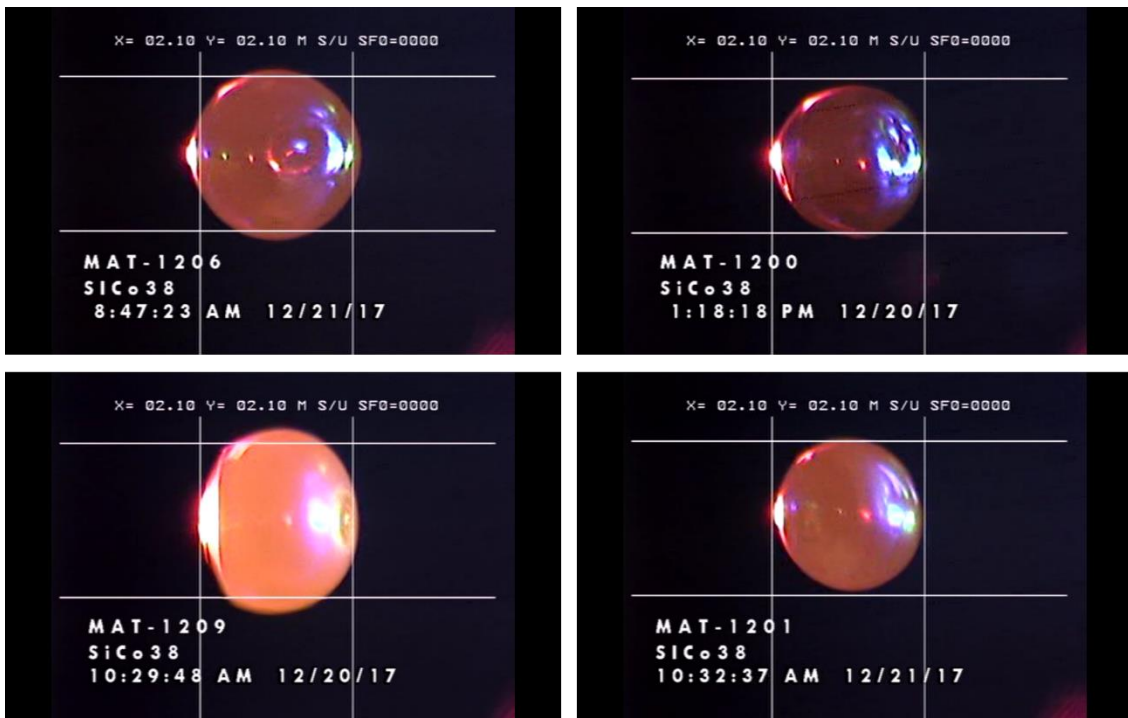


Figure 6. Four unique samples that remain within the digital box. The dimension of the box reads $x = 2.20$ mm and $y = 2.20$ mm and remains fix in position.

The burn paper method was used to determine if the heating laser hit the samples in the same location on every sample. A thin steel mesh provided by NASA was wrapped around the plunger stem that loads individual samples within the chamber. This mesh

functions as a location indicator on where the laser beam is aimed. Zr control sample is levitated and heated. Raw images files from the video clip are taken and superimposed to visually determine that the sample is heated along its equatorial plane. The laser remains fixed its orientation. Figure 7 shows how the setup is performed to ensure the laser beam is properly aligned to strike the samples along the sample's equator and provide symmetric heating during processing.



Figure 7. (top) Steel mesh is wrapped around stem to act as a burn indicator. The hole shows the location where the laser hit the mesh. (middle) Zr sample is levitated and exposed to the heating laser. (bottom) Top and middle images are superimposed to visually determine how the laser is oriented to the samples' equatorial plane.

The ESL facility utilized a 200 W YAG laser and provided corresponding power levels as a function of input voltage. A plot of the Power [W] as a function of voltage [mV] was then interpolated which can be seen in Figure 8.

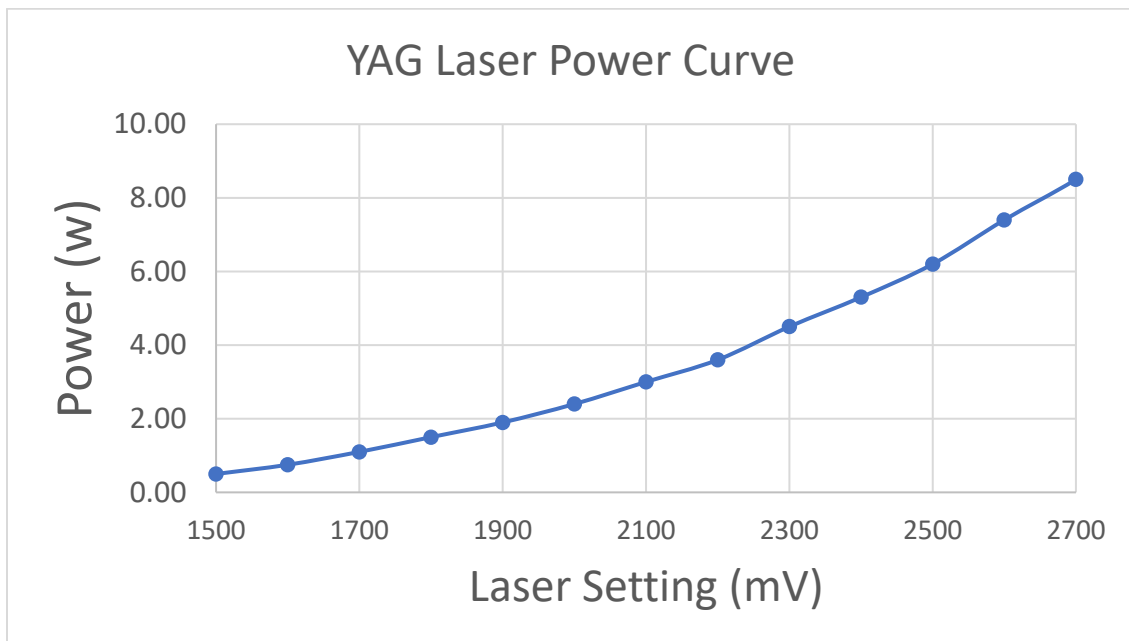


Figure 8. Power curve of the YAG laser. The voltage level corresponds to the output energy.

Based on the power curve, two laser settings were calculated and selected to ensure the samples undercooled below the 2nd recalescence temperature. For this study, the determined level of laser power was 2.4 W and 0.5 W which corresponds to laser

voltages of 2000 mV and 1500 mV respectively. A 2700 mV setting corresponds to 8.4 W which is the energy required for the sample to reach the liquidus temperature.

It is also important to note that the heating rate is not entirely absorbed by the samples due to reflection of radiation. A system of equations was used to determine the fraction absorbed compared to the total output of the laser. The following equations (5) and (6) were used to determine (q_{laser}), the heat transfer rate absorbed by the sample [W] for the two laser settings and the control ground Laser Off:

$$q_{laser} = mC_p \left(\frac{dT}{dt} \right) - q_{rad} \quad (5)$$

$$q_{rad} = \sigma \varepsilon A (T^4 - T_{env}^4) \quad (6)$$

where m represents the mass of the alloy sample [mol], C_p is the specific heat (~ 42

$\frac{J}{mol K}$) [46], $\frac{dT}{dt}$ is the heat rate [K/s], q_{rad} is the heat loss through radiation

[J/s or W], σ is the Stefan Boltzmann constant ($5.67E-8 Wm^{-2}K^{-4}$), ε is the emissivity, A is the surface area of the sample [m^2], and T^4 is the temperature to the fourth power [K^4].

The energy rate, q_{laser} absorbed into the 30 mg ($3.44E-4 mol$) sample with a 1mm radius with laser set to melt the sample was calculated at (2.2 W out of the 8.4W). This was determined by solving equation (1) above under the condition of the laser is off

($q_{laser} = 0 W$) and cooling rate, $\left(\frac{dT}{dt} \right)_2$ (heat rate loss), evaluated at the peak

temperature to which the emissivity was calculated in equation (2) and used in equation (1) with the heating rate $\left(\frac{dT}{dt} \right)_1$ heat rate gained. A schematic of a typical melt cycle used

in evaluating the heating rate of the laser is shown in Figure 9. The peaks represented by the blue line in the figure is the end of the superheat phase and the beginning of the cooling phase. The secondary axis show the reduction of voltage to both V1 and V2 corresponding to LOW and HIGH. The slope of the temperature profiles indicate the change in heat loss rate due to the continual addition of energy. The calculated emissivity ($\varepsilon \cong 0.22$) for CoSi is assumed to be constant for the remaining calculations for the absorbed Low and High laser settings. Equation (1) and (2) is used to find the approximate fraction of power absorbed by the laser during the cooling phase of the melt cycle. $\left(\frac{dT}{dt}\right)_2$ is used from the thermal profiles and q_{laser} is the calculated. The fraction absorbed by the sample for the Low and High settings are 0.11 W out of 0.5 W and 0.52 W out of 2.4 W respectively. These calculated values will be used for future work in magnetohydrodynamic modeling to determine the convection rate as a function of power input.

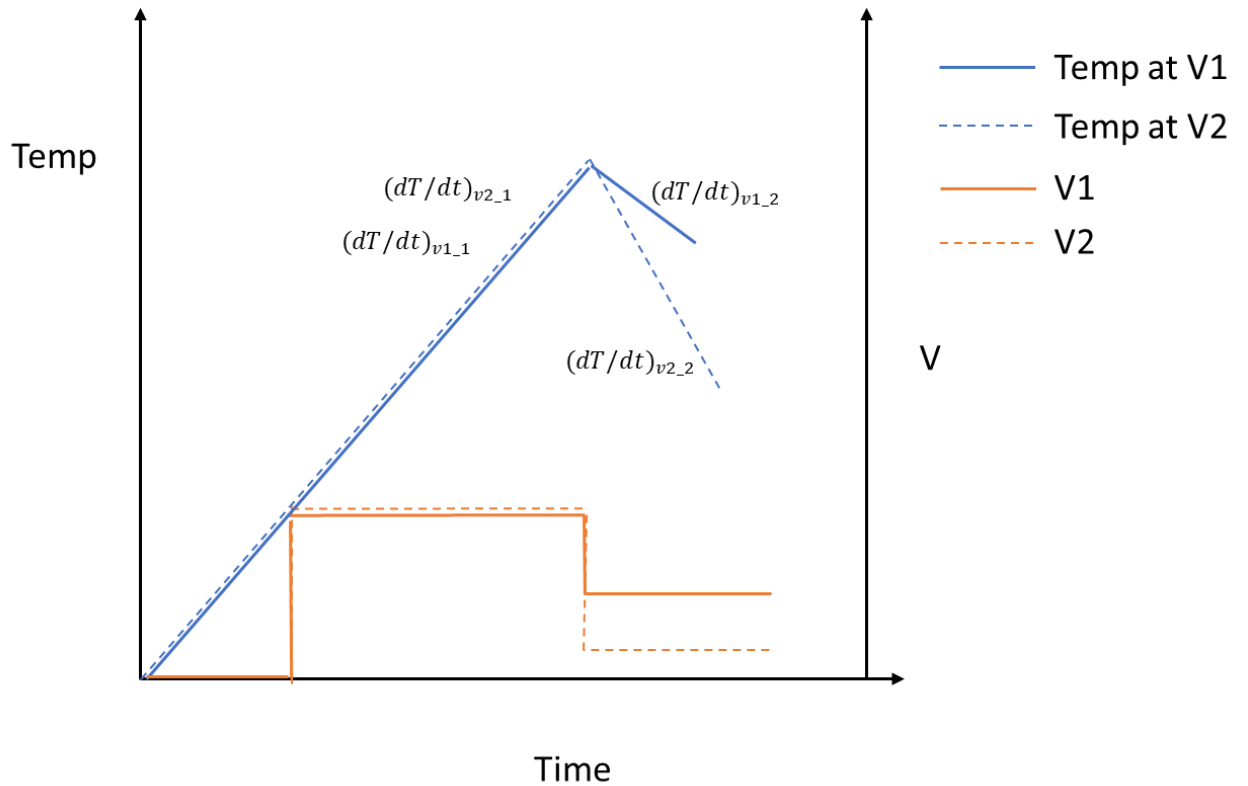


Figure 9. Plot of Temperature and Voltage as a function of time in determining the fractional absorbed heating rate of the YAG laser in both voltage settings.

Image Processing

Scanning Electron Microscope

Post-processed samples were then imaged for their surface microstructures using a Phenom Pro-X Scanning Electron Microscope (SEM) at the Nanomaterials Lab at Tufts University. To scan the surface area of the samples, the Motorized tilt and rotation base insert was used. The tile and rotation insert has a maximum tile of 45 degrees and a continuous 360 degree rotation. Figure 10 shows the motorized tilt component insert.



Figure 10. (left) The Phenom Pro-X SEM. (right) The motorized tilt/rotation base insert component. The base is capable of 360 degree rotation and a maximum 45 degree tilt.

Multiple images were taken for each sample. The images saved were 1024x1024 pixels. The scale ratio of pixel length to field of view (FOV) was used to determine the actual length of each pixel. It is important to factor in the scale ratio as images can differ in magnification. At low ΔT , white contrasted pixels correspond to the primary CoSi particles. The surrounding dark contrast are the CoSi₂ coarsening grains that developed during the 2nd recalescence. Greater ΔT will exhibit CoSi₂ as the primary phase (dark pixels) with CoSi particles (white) forming through the dendrites. Figures 11 and 12 show SEM images of CoSi62% at different undercoolings with clear differences in microstructure. Discriminating areas of CoSi and CoSi₂ for each image was accomplished using National Instrument's Vision Assistant.

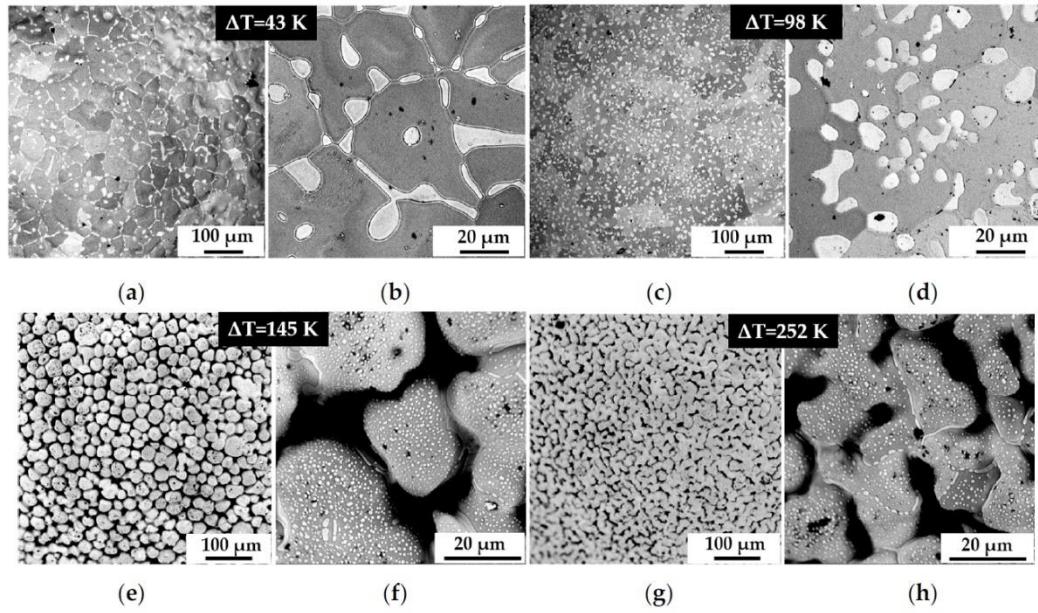


Figure 11. Back-scattering SEM images of the CoSi microstructure. a-b) & c-d) show CoSi as the primary phases (white pixel contrast) with the surrounding CoSi₂ coarse grains (dark pixels). e-f) g-h) show CoSi₂ as the primary phase.

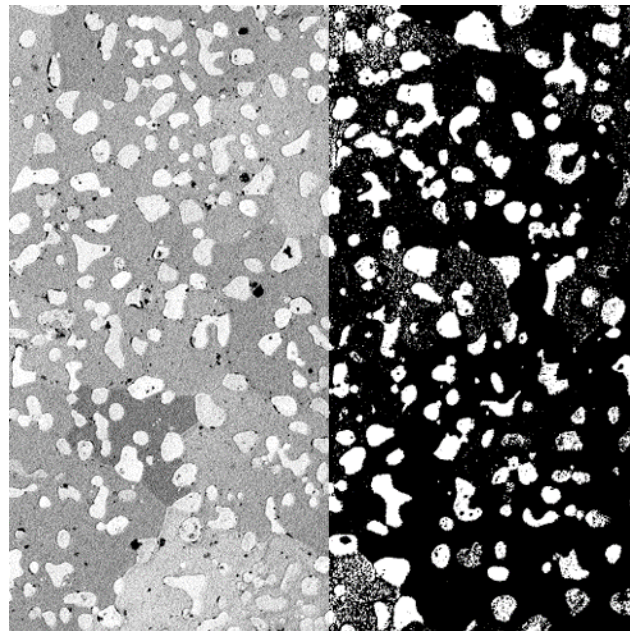


Figure 12. A partial processed SEM image. The CoSi particles (white pixel contrast) are identified (left) converted to a binary image (right).

Vision Assistant

Vision Assistant offers a variety of tools to enhance, redact, and identify desired objects in images. In this study, the primary phase is identified and measured to be compared with the other groups. Figure 13 shows the front panel of Vision Assistant and the road map of the processing functions. The measurement of the radii of the dendrite heads followed a common process although few images required additional image manipulation to improve the distinction between primary and secondary phases and voids.

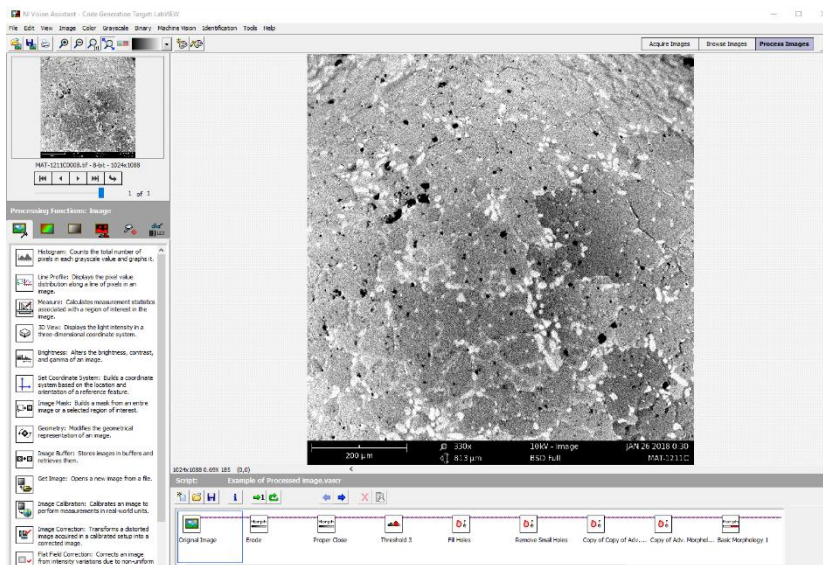


Figure 13. Vision Assistant with an SEM image with the script of functions to identify the primary phase which is the white portions in this particular image. A detailed script is explained in the appendix part C.

Data Analysis

It is important to consider composition shifts after primary recalescence. Depending on amount of undercooling, the primary recalescence may result in the remaining melt as either Co-rich or Si-rich. Thus, the recalescence temperature which the TR1 reaches will not be the liquidus temperature of CoSi₆₂ instead, the new melt plateau is shifted below the equilibrium eutectic line as seen in Figure 14. The new (TR1') can be calculated with the Stefan's equation (7), the lever rule, and an extrapolated equations from the phase diagram:

$$C_p \Delta T = f_s \Delta H_f \quad (7)$$

where C_p is the specific heat, ΔH_f is the heat of fusion, and f_s is the fraction solid formed. The Stefan's equation predicts the fraction solid formed based on undercooling of a given material. Table 1 displays the thermophysical properties of CoSi and CoSi₂. C_p is assumed to be constant for both.

Table 1. Thermophysical Properties of CoSi and CoSi₂ [45]

CoSi	CoSi ₂
$C_p = 42 \left[\frac{J}{mol K} \right]$	$C_p = 42 \left[\frac{J}{mol K} \right]$
$\Delta H_f = 32192 \left[\frac{J}{mol} \right]$	$\Delta H_f = 35678 \left[\frac{J}{mol} \right]$
$T_L = 1733 [K]$	$T_L = 1593 [K]$

The lever rule (8) is used to determine the f_s as the eutectic CoSi₆₂ alloy has two terminal compositions:

$$f_s = (w_o - w_l)/(w_s - w_l) \quad (8)$$

where w_o is the eutectic composition (0.625), w_s is the fraction of primary phase, and w_l is the fraction of secondary phase. An extrapolated equation from the phase diagram in Figure 15 and 16 represent the assumed equilibrium line for CoSi and CoSi₂: Here, the theoretical equilibrium temperature of (T_L) at resulting Si compositions can be calculated with the metastable extended equilibrium line (9) and (10).

$$T_{L_{CoSi}} = m_{L_{CoSi}}(w_l) + 2317 \quad (9)$$

$$T_{L_{CoSi_2}} = m_{L_{CoSi_2}}(w_l) + 1408.4 \quad (10)$$

where ($m_{L_{CoSi}} = -1168 \left[\frac{K}{at.\%} \right]$) and ($m_{L_{CoSi_2}} = -285.71 \left[\frac{K}{at.\%} \right]$) are the internal liquidus slope. The T_L values can be correlated with the undercooling ΔT range. Utilizing these three equations, the corrected undercooling (ΔT_{Obs}) for the new recalescence temperature of the shifted composition can be determined:

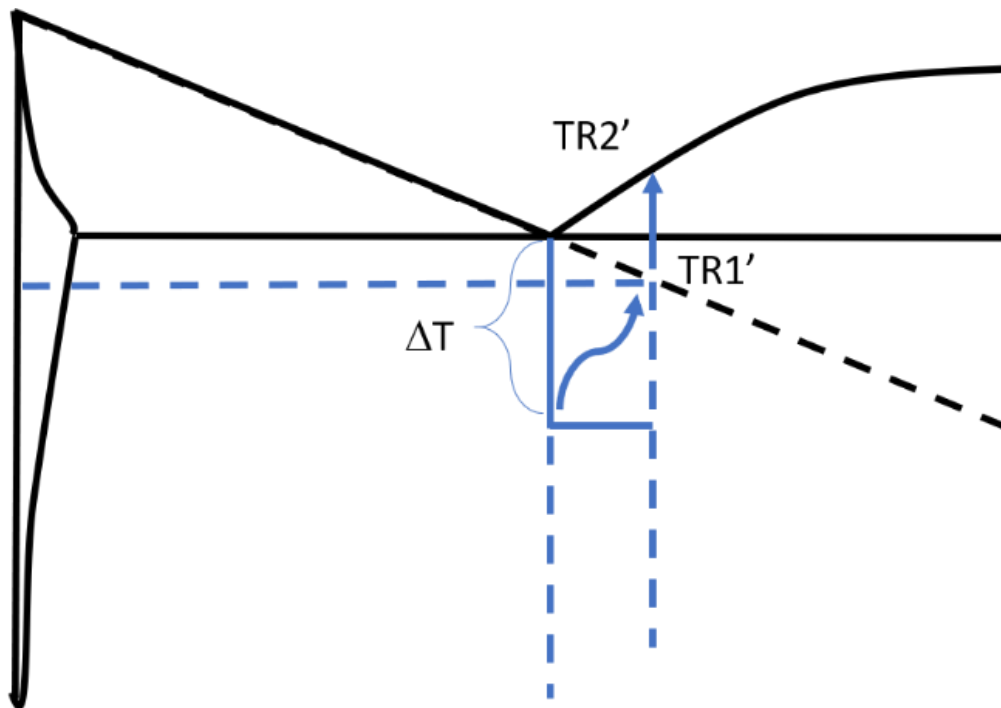


Figure 14. Recalescence temperatures due to shift in composition. TR1' is the new melt plateau for primary CoSi phase. The TR2' is the new melt plateau for the second recalescence.

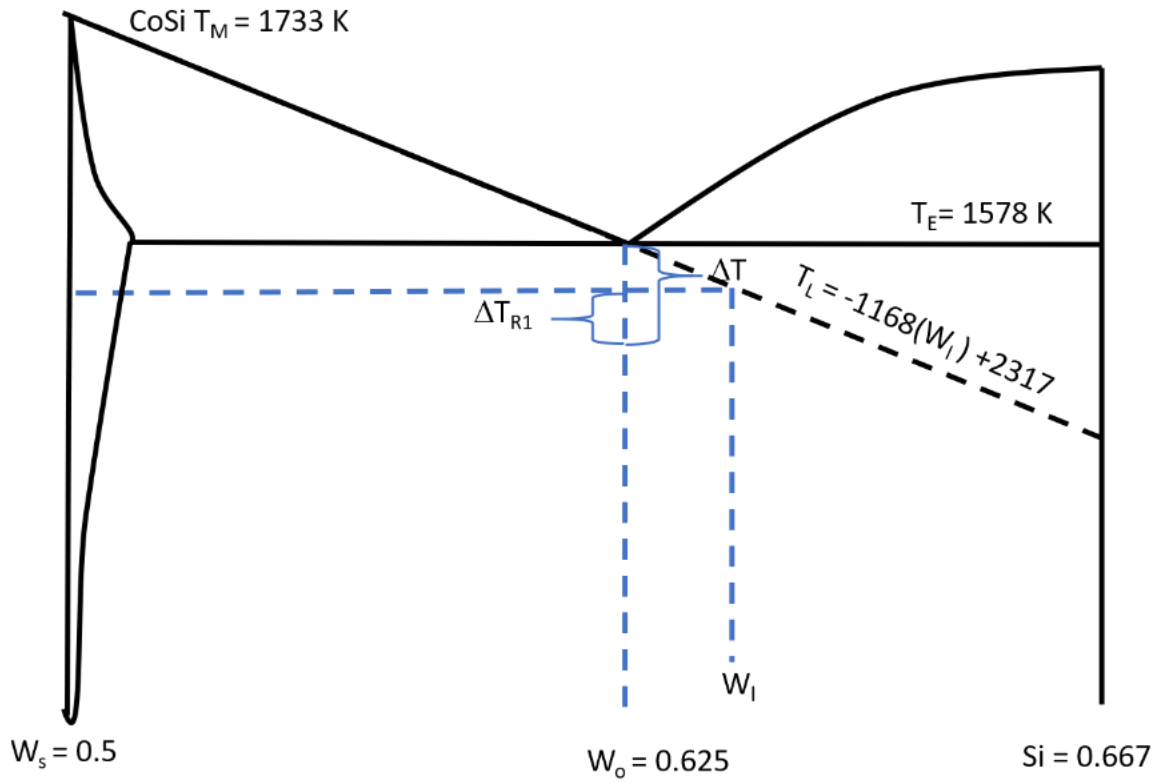


Figure 15. Phase diagram with key points to address the shift in composition due to recalescence and the resulting melt plateau for primary CoSi.

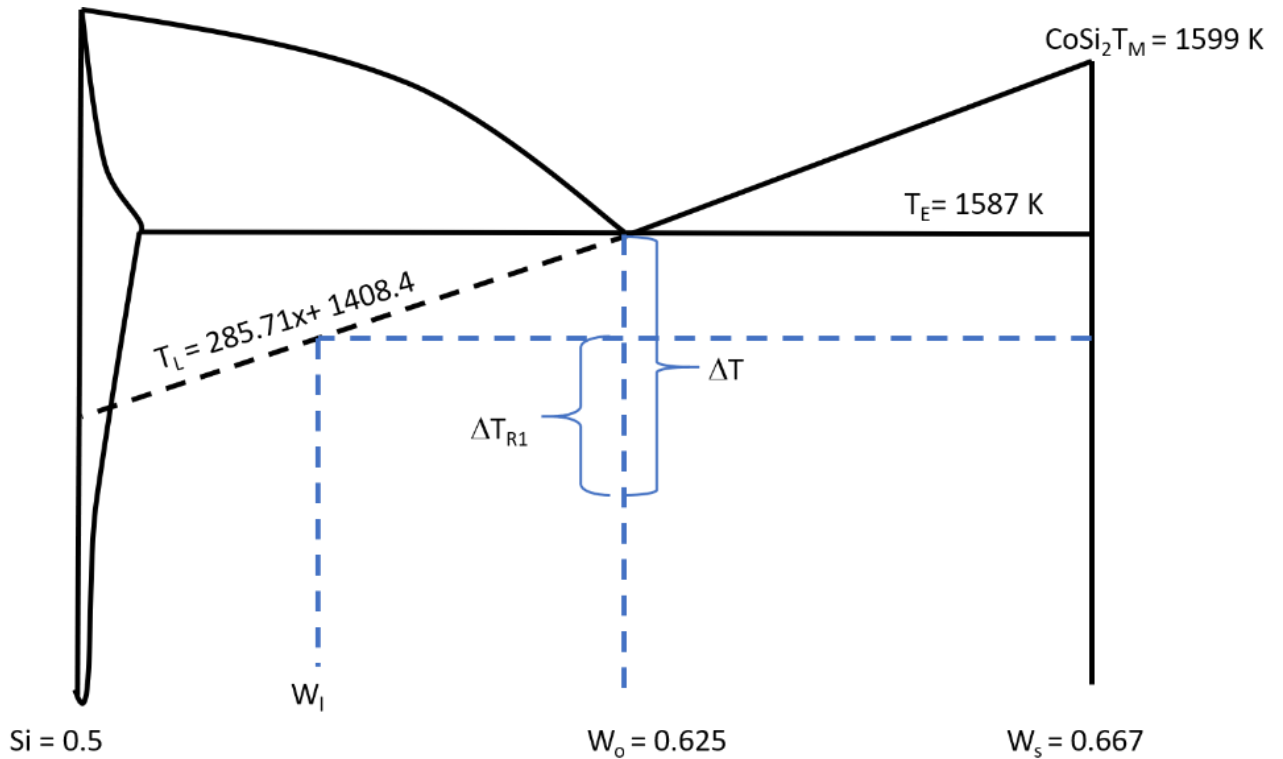


Figure 16. Phase diagram with key points to address the shift in composition due to recalescence and the resulting melt plateau for primary CoSi₂.

An undercooling value of 636 K must be achieved in order for the Si mole concentration in the remaining melt to reach 50 at. % Si. This value was calculated with equations (7) and (8); $w_l = 0.5$. As mentioned earlier, ($\Delta T \sim 100$ K) is the transition of primary phase from CoSi to CoSi₂. Because the phase competition between the two is unclear at this degree of undercooling, the range of mole fraction that is potentially involved is $w_l = [0.6193, 0.6436]$. This concentration difference results in 2% which is determined as the acceptable range for processed samples. Any samples with a 2%

mass difference are thus discarded from the study. All remaining samples are then corrected for the new recalescence temperature.

To determine if continual internal convection provides enough force to wash away the rejected solute in the path of the developing dendrites [47, 48], this study will continue to utilize the methodology in Jeon and Matson [3] using the NASA-MSFC ESL experimental facility [8]. The laser will continue to provide energy at a lower power setting allowing the alloy to solidify but simultaneously provide energy to continue internal convection. If the hypothesis is true, the CoSi₆₂ samples will display finer grain sizes the greater the laser energy input. The control group will be samples that have the laser setting to off once the sample is molten. Surface images provide means to determine the grain sizes of the CoSi and CoSi₂ regions.

All processed samples are then analyzed for their surface structures. Each image was manipulated to enhance the contrast between the two eutectic phases and contaminants (black pixels). The primary structure is identified for all images. Primary CoSi is identified as white contrasted pixels while primary CoSi₂ is identified as the gray contrasted pixels in large clusters. Images display the Field of View (FOV) as the magnification changes to acquire the ratio of actual length to pixels. All images are saved as 1024x1024 pixel image. If the FOV displays 268 μm , then 1 μm is equivalent to 3.82 pixel lengths or 14.6 pixels per $1\mu\text{m}^2$. Due to the curvature of the dendrite head for primary CoSi₂, the visibility of the structure diminishes as you reach the radial ends. To account for this issue, a histogram of the pixel value distribution of a selected image was generated in Figure 17.

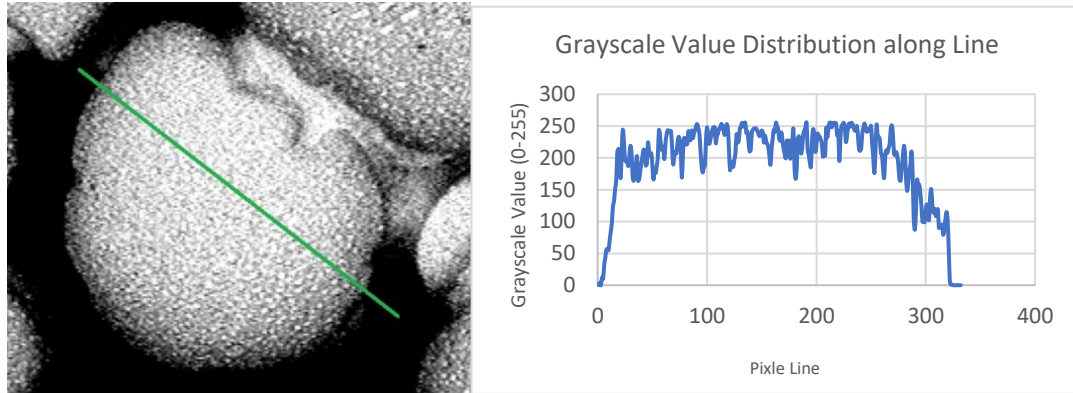


Figure 17 (left) shows the dendrite head with the drawn line (in green) that measures the pixel value along the Pixel line (same green line) which is plotted (right).

An additional histogram was taken over a line drawn across a dendrite head relating the pixel value as a function of position. A threshold range between the peak pixel value to the point of inflection was selected as the best approach in separating the solidified CoSi alloy and the liquidous “black-void” region. For this particular image, the threshold values were (91-170). Identifying the radius of the circle was carried out by the number of pixels detected in the “blob detection”. To keep a consistent measurement for all images, the maximum size circle to fit within each blob is identified. Therefore it is expected to get a slightly lower value of radii. This is a weakness of the image processing technique. Manual correction is needed as multiple circles were identified within the same dendrite head. Figure 18 is an example of the circle detection for identified dendritic heads. An excel file reports the radii in pixels. The average is taken along with standard deviation.

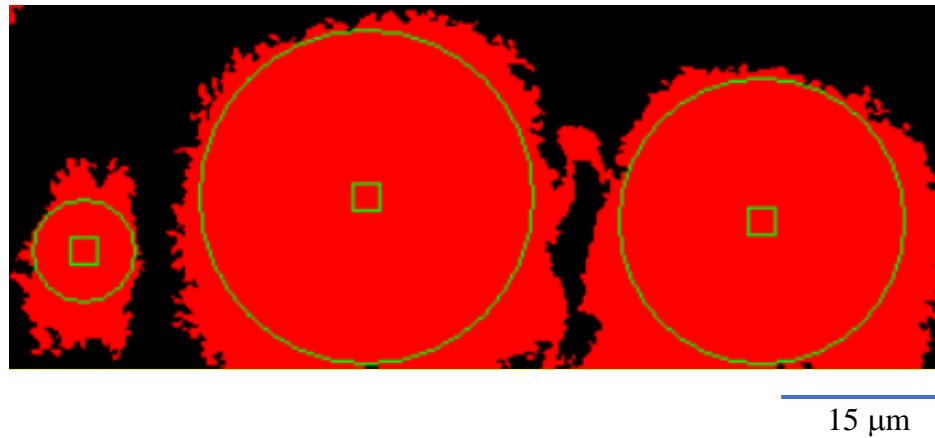


Figure 18. Circle detection function in Vision Assistant applied to a binary image. A maximum circle is fitted within the “blobs” of the binary image.

Further image analysis was conducted to compare the fraction of solid formed for each primary phase in respect to the entire image. Vision Assistant’s % area detection in particle analysis detects the number of active pixels in the image compared to the total number of pixels. The average is then taken with a standard deviation for all images. This data is expected to correlate with the Stefan’s equation for the fraction of solid phase as a function of undercooling. Undercooling has a direct relationship with the solid fraction; therefore it is expected to see an increase in % area with increased undercooling.

4 Results

The following data was gathered entirely at the ground ESL facility at NASA – MSFC. The goal for thermal processing was to obtain a range of undercooled samples with laser treatment as means to compare with the laser off group; however, no deep undercooling values ($\Delta T > 100$ K) for laser treated samples were reached for this study. Therefore, no laser treated groups are represented for Figure 20. Also, a nine samples were unable to be complete the melt cycle process, and these samples were not considered in the results.

Figure 19 shows the average dendrite tip radii for CoSi62 with CoSi as the primary phase. Comparing the laser power settings: (0 W= Laser Off, 0.5 W = Low, and 2.4 W = High) there are clear differences in radii as the circulation is increased between low and high settings. The laser off group reveals a negative linear correlation with an initial large radii for small undercooling values ($\Delta T < 20$ K).

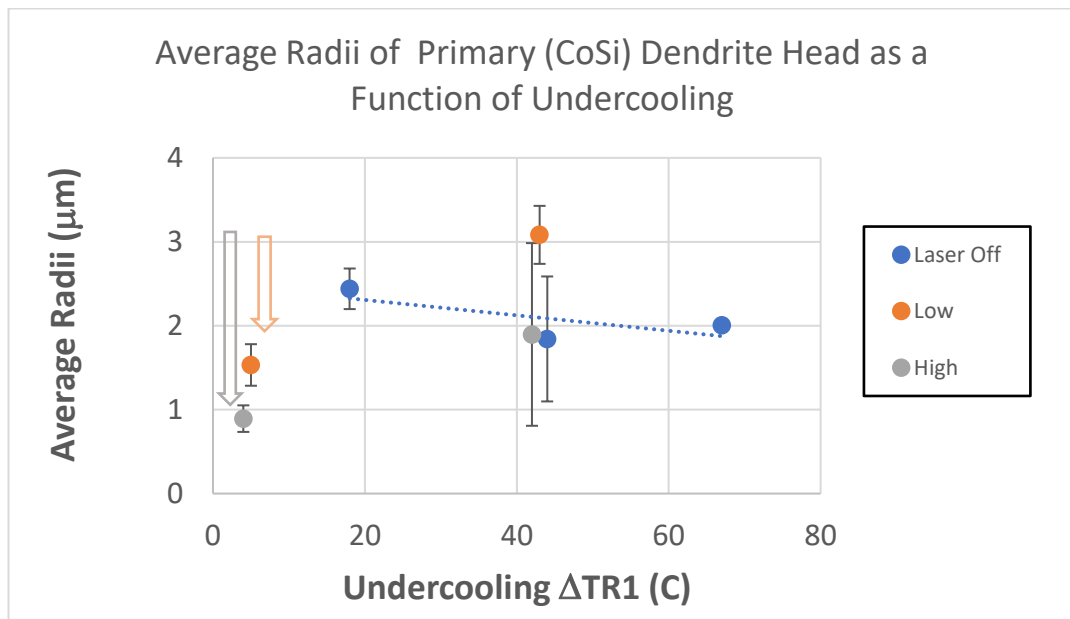


Figure 19. Plot of average dendrite tip radii as a function of undercooling for CoSi phase.

Figure 20 shows the average dendrite tip radii for CoSi₆₂ at % alloy with CoSi₂ as the primary phase as a function of undercooling of only the Laser Off group. The figure clearly shows a negative linear correlation with initial radii greater than its alternative phase ($r = 8 \mu\text{m}$).

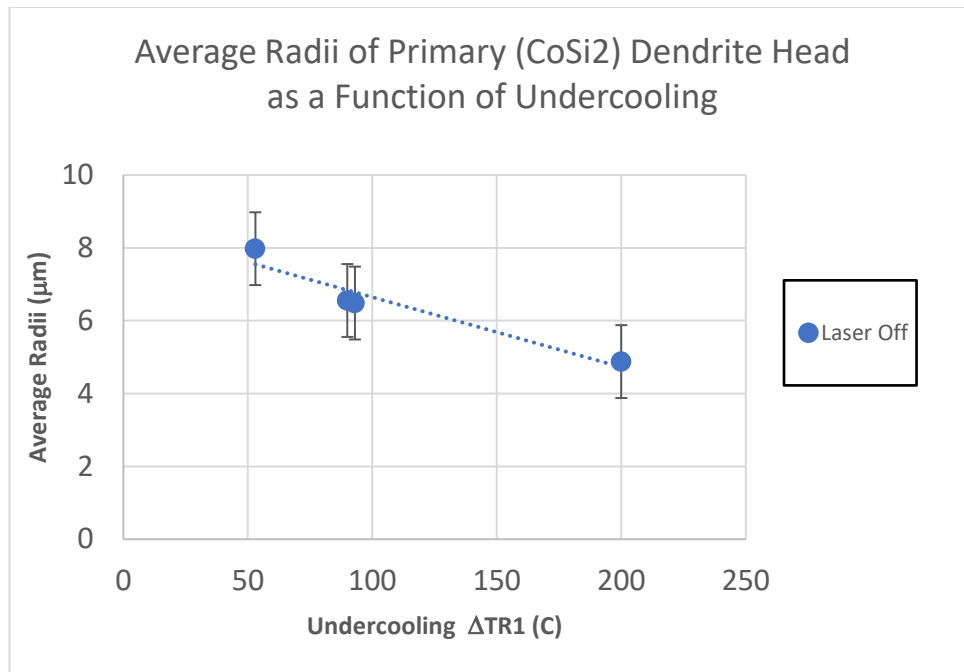


Figure 20. Plot of average dendrite tip radii as a function of undercooling for CoSi₂ phase for only Laser Off group. No deeper levels of undercooling for laser treated groups were reached.

The error bars in both plots are due to the variation in radii in multiple SEM images taken from each sample. The average radii was determined, and the standard deviation is accounting all the images per sample. The number of images for each sample range

from (4-6). Figure 21 shows the average percent area covered in the binary image of CoSi₆₂ with CoSi as the primary phase. Figure 18 shows the average percent area covered with CoSi₂ as the primary phase. The plot compares the same sample groups.

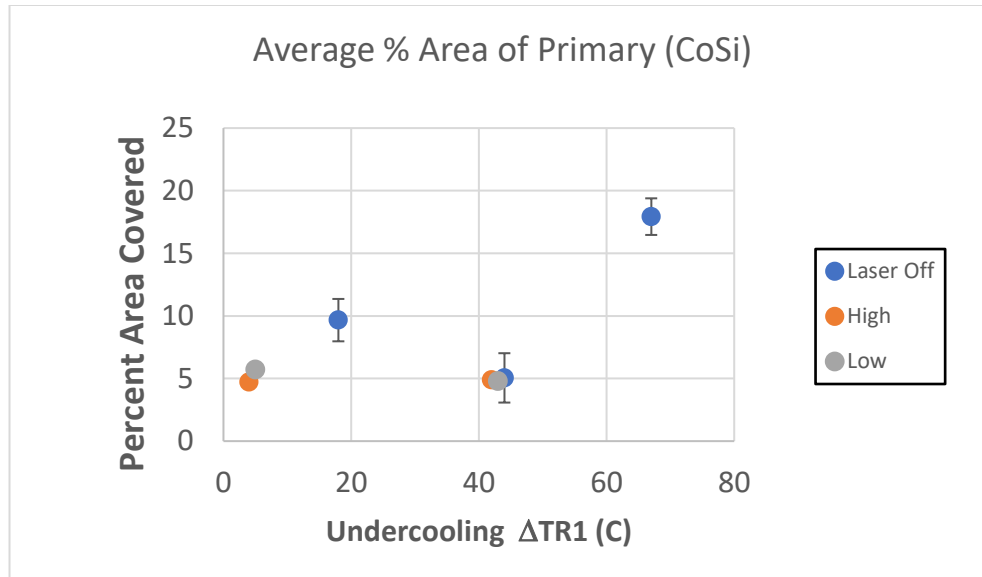


Figure 21. Plot of average % area as a function of undercooling for CoSi phase.

Both High and Low laser settings settle along 5 % with increasing undercooling.

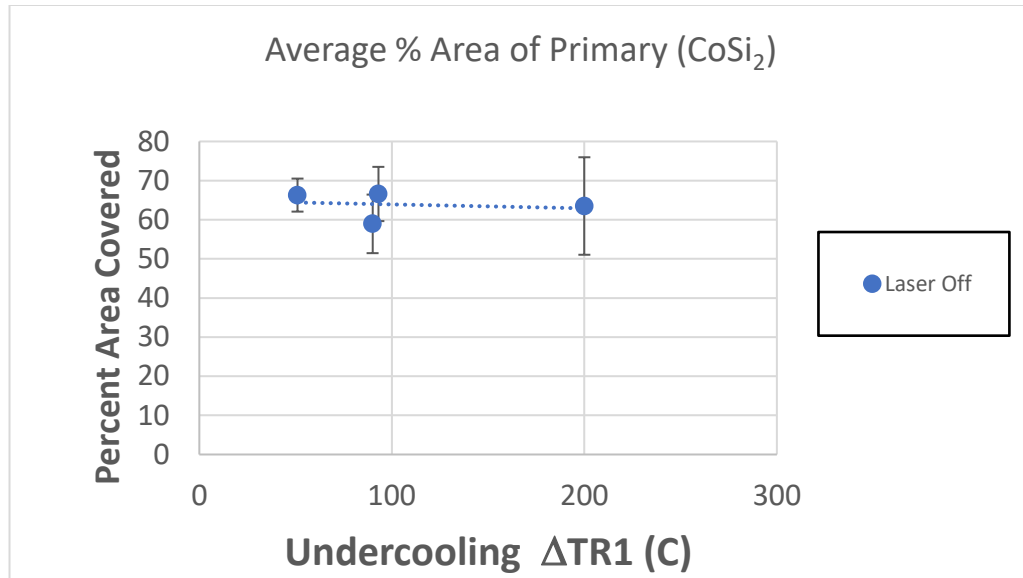


Figure 22. Plot of average % area as a function of undercooling for CoSi₂ phase.

The plot of % area for primary CoSi₂ appears to settle along 60-70% for ($\Delta T > 100$ K).

Figures (23- 26) show a distribution of the radii of single images detected with Vision Assistant. The radii were converted from the number of pixels base on the scaling factor.

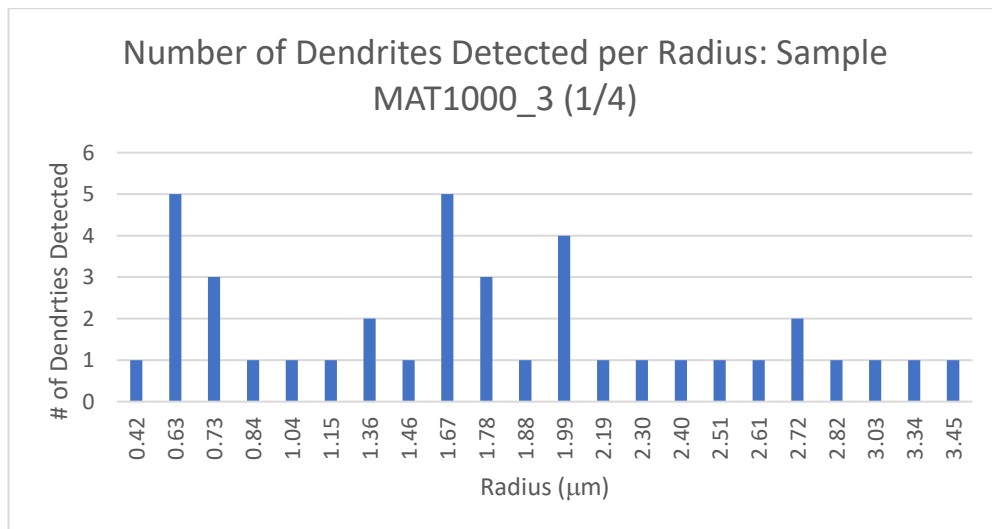


Figure 23. Distribution of # of Radii from single image of sample MAT1000_3(1/4)

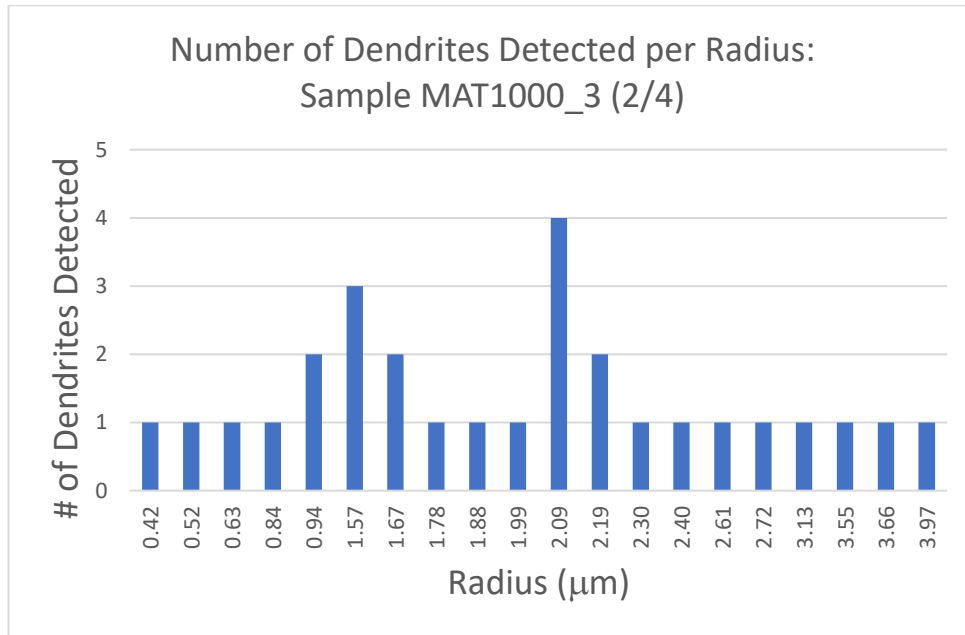


Figure 24. Distribution of # of Radii from single image of sample MAT1000_3(2/4)

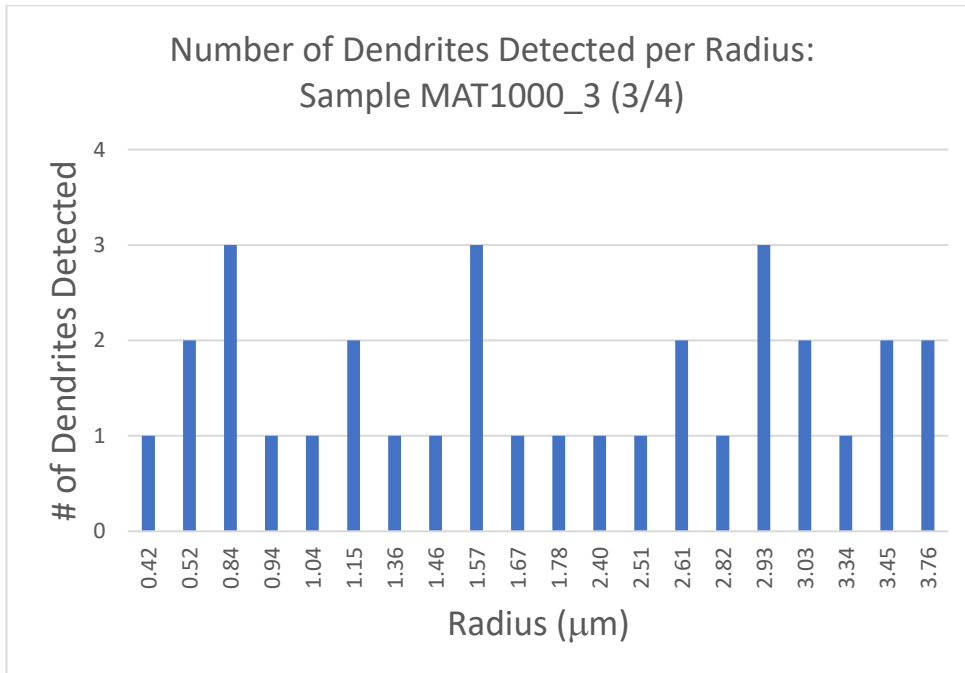


Figure 25. Distribution of # of Radii from single image of sample MAT1000_3(3/4)

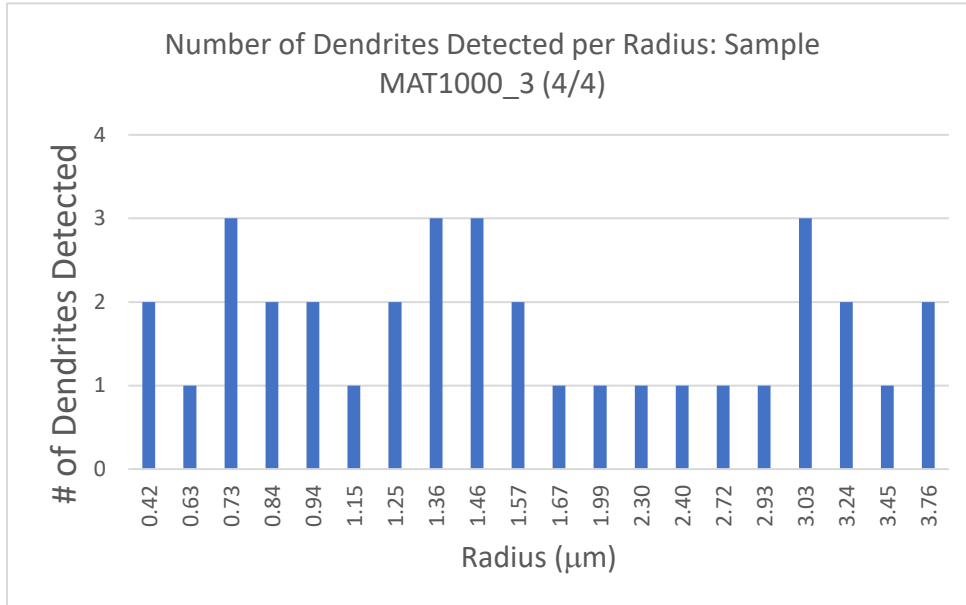


Figure 26. Distribution of # of Radii from single image of sample MAT1000_3(4/4)

5 Discussion

Depending on degree of undercoolings ($\Delta T \neq 100$ K) the Si compositions shifts either right Figure 15 or left Figure 16 and thus the recalescence temperature is shifted below the equilibrium eutectic line. For deep levels of undercooling for primary CoSi_2 , the calculated value of the true melt plateau did not change significantly near the eutectic composition. For a ($\Delta T = 100$ K) the calculated melt plateau is $T_L = 1585.6$ K. For shallow levels of undercooling, the extrapolated equilibrium temperature for CoSi is steeper compared to CoSi_2 . In the case that primary CoSi is formed the calculated new melt plateau at ($\Delta T = 100$ K) is 1565.09 K. Lower undercoolings are corrected for new recalescence points.

The average radii range for primary CoSi_2 is greater compared to the CoSi phase.

As predicted with the LKT theory, the average dendrite tip radii decreases with increased undercooling in both in CoSi and CoSi_2 in Figure 15 and 16 for no laser setting. There is no low undercooling for CoSi_2 phase as expected in Jeon and Matson [3] The thermodynamic driving force that builds with increasing undercooling clearly show the expected negative trend. Because the LKT theory is independent of internal convection, the growth velocity of the primary phase become the dominate force and therefore fluid flow effects are minimal. When the laser group is introduced, there is an unexpected correlation which is not expected from LKT theory. The high voltage settings for this study was selected to ensure that the molten sample was able cool below the 2nd recalescence temperature and simultaneously continue Marangoni effects. The low voltage was chosen to be the lowest power setting the YAG laser can output. These processing parameters reveal a clear positive trend with increase in undercooling.

Looking at the high voltage setting, the plot is nearly shifted down with an identical slope as the low voltage setting. At low undercooling for primary CoSi the average radii drops with stirring. This suggests that at low undercooling ($\Delta T < \sim 20$ K) the growth velocities are low and minimal compared to the fluid flow so fluid flow effects dominate. This effect is more profound with increased laser power.

At higher undercooling ($\Delta T > \sim 20$ K), the for primary CoSi phase is not expected to produce laser-treated samples with greater radii because growth velocities dominate over the fluid flow effects. Obtaining higher undercool samples with laser treatment will determine this claim.

Figures 21 and 22 reveal trends that do not agree with Stefan's equation which predicts that the fraction of solid form is proportional to the undercooling. With increasing undercooling, the average % area should also increase revealing a positive linear trend. The average % area for primary CoSi₂ are greater than that of primary CoSi. The % area of primary CoSi₂ in Figure 22 does not vary with undercooling following this image processing technique.

The strengths of this developed imaging technique is the complete identification of all complete primary phases in the images. Dendrite heads that are cut on the border of the image are ignored. The distribution of radii is not an exact reflection of the entire sample as only sections of the sample could be imaged. An entire scan of the sample is not feasible for this study. Few weaknesses are present in the image processing technique. The oblong shapes in the surface images of both primary phases of CoSi and CoSi₂ are assumed to be circular in shape. A second assumption is the pixel value range determined to be identified in the threshold function. High quality SEM images relies

on good intuition in the image manipulation process. This includes manually controlling brightness, contrast and focus which are adjusted differently for all samples. The selected threshold to identify the primary phase can pick structures that are not considered as part of the primary phase. This includes reflection of light on CoSi_2 structures which is then mistaken as CoSi structures.

6 Conclusions

The goal of this study was to develop a new technique to evaluate the decanted surface microstructures of metallic alloys. To show clear changes in grain and dendrite head sizes, CoSi₆₂ alloys were selected due to its large partitioning at the eutectic composition. To acquire decanted surface structures, samples are undercooled to rapidly solidify and form these grain and dendrite structures of various sizes. In addition, convection is also explored as the rejected solute particles during partitioning remain in the metastable phase. With this system, undercooling and convection rates are explored in this study. Dendrite growth theory is expected to reveal a trend of decreasing dendrite sizes continues as undercooling levels increase. Dendrite sizes should also decrease as convection rates increase at lower undercoolings because growth velocities are not as strong. Both trends were seen in the results. The developed imaging technique was able to produce these plots when identifying the primary phases.

Phase Diagram

- Primary undercooling does not influence recalescence temperature for primary CoSi₂ even with the significant shift in composition of the remaining liquid as predicted by the Stefan Equation and the metastable extension of the Equilibrium Phase Diagram. Primary CoSi is sensitive to the shift in composition and must factor in the new recalescence temperature.
- An undercooling of 636 K shifts the curve to the far left for a 50% Si concentration reaching the terminal eutectic phase. This undercooling is infeasible under standard operating conditions and thus we will always have concentrations in the liquid remaining after primary recalescence that are near to the eutectic composition regardless of primary undercooling.

- At ($\Delta T = 100$ K), Si composition in the remaining melt is ($w_l = 0.619$) for primary CoSi_2 , and Si composition becomes ($w_l = 0.643$) for primary CoSi. Both do not deviate much from the initial eutectic compositions.
- At ($\Delta T = 100$ K), the shifted recalescence temperature becomes ($T_L = 1585$ K/ $\Delta T = 2$ K) and ($T_L = 1565$ K/ $\Delta T = 22$ K), for CoSi_2 and CoSi respectively.

Decanted Images

- High undercooled samples resulted in CoSi_2 and SEM images revealed surface decanted structures due to the removal of liquid toward the center.
- Diameter of dendrite as a function of undercooling decreases for primary CoSi_2 and CoSi for Laser Off case.
- Mass fraction as a function of undercooling does not agree with the calculated fraction solid with Stefan's equation when estimated using the surface decanting analysis procedure.

Image Technique

- The developed image processing technique proves applicable to the evaluation of the decanted surface structures. Minimal source of error stems from the varying oblong shapes of the dendrite heads with limited images to represent the whole sample.

Convection

- Comparing applied power to absorbed power shows that 0.52 W out of 2.4 W are absorbed during melting at the high laser setting while 0.11 W out of 0.5 W were absorbed during the low laser setting.
- Dendrite diameters change significantly at low undercoolings indicating convection effects are significant.

7 Future Work

Several areas of this project can be strengthened with some expansion to support the interpretation of the results. First, there is a lack of laser treated samples with medium and deep undercooling. This gap may be due to contamination. Samples are exposed to any number of potential contaminants throughout the preparation process even until the superheat treatment prior to the melt cycle. It is possible that the quality of the arc-melting process may significantly influence contamination levels (oxides) within the sample. These contaminants greatly jeopardizes the chance for the CoSi₆₂ to reach deeper ΔT . Best course of action to aim for deep undercoolings is improving the preparation of CoSi samples.

Second, quantify the convection rates with power input. Calculating the convection rates requires thermodynamic modeling which requires measurements of surface tension, viscosity, shear rates, etc. By quantifying the stirring rates as a function of energy input, it is possible to predict the size of the grains.

Third, apply the LKT theory with the assumption of CoSi as a diluted alloy to validate the declining radii trend as a function of undercooling. The projected slope comparing average radii and level of undercooling will be applied to the laser-treated group. The continuation of this study will provide insights to further processing parameters for future sample testing.

Fourth, improving the image processing technique to accurately identify the primary structures. There are additional image processing functions in recent versions of National Instrument's Vision Assistant that may provide alternative ways to detect the extent of the grain sizes without the threshold function which relies on the pixel

intensity value. In addition, expanding the assumption of a circular dendrite head to ellipses and account for the equatorial and axial radii will potentially increase the accuracy of the results.

8 References

- [1] B. Linzer, G. Hohenbichler, S. Bragin, G. Arth, and C. Bernhard, "Experimental simulation of the solidification of steel at higher cooling rates," *BHM Berg-und Hüttenmännische Monatshefte*, vol. 154, p. 498, 2009.
- [2] M. Li, K. Nagashio, T. Ishikawa, A. Mizuno, M. Adachi, M. Watanabe, *et al.*, "Microstructure formation and in situ phase identification from undercooled Co–61.8at.% Si melts solidified on an electromagnetic levitator and an electrostatic levitator," *Acta Materialia*, vol. 56, pp. 2514-2525, 2008/06/01/ 2008.
- [3] S. Jeon and D. M. Matson, "Formation of Cellular Structure on Metastable Solidification of Undercooled Eutectic CoSi-62 at.%, " *Crystals*, vol. 7, p. 295, 2017.
- [4] J. T. McKeown, A. K. Kulovits, C. Liu, K. Zweiacker, B. W. Reed, T. LaGrange, *et al.*, "In situ transmission electron microscopy of crystal growth-mode transitions during rapid solidification of a hypoeutectic Al–Cu alloy," *Acta Materialia*, vol. 65, pp. 56-68, 2014/02/15/ 2014.
- [5] D. M. Matson, "Nucleation Within the Mushy Zone," *Solidification of Containerless Undercooled Melts*, pp. 213-238, 2012.
- [6] D. M. Herlach, T. Palberg, I. Klassen, S. Klein, and R. Kobold, "Overview: Experimental studies of crystal nucleation: Metals and colloids," *The Journal of Chemical Physics*, vol. 145, p. 211703, 2016.
- [7] J. Rogers, M. Robinson, L. Savage, W. Soellner, and D. Huie, "An Overview of the MSFC Electrostatic Levitation Facility," 1999.
- [8] J. Rogers and M. Sansoucie, "Containerless processing studies in the msfc electrostatic levitator," in *50th AIAA Aerospace Sciences Meeting including the New Horizons Forum and Aerospace Exposition*, 2012, p. 924.
- [9] T. Lida and R. Guthrie, "The Physical Properties of Liquid Metals, Clarendon," ed: Oxford, 1988.
- [10] G. Wille, F. Millot, and J. Rifflet, "Thermophysical properties of containerless liquid iron up to 2500 K," *International Journal of Thermophysics*, vol. 23, pp. 1197-1206, 2002.
- [11] S. Lee, W. Jo, Y. c. Cho, H. H. Lee, and G. W. Lee, "Solution electrostatic levitator for measuring surface properties and bulk structures of an extremely supersaturated solution drop above metastable zone width limit," *Review of Scientific Instruments*, vol. 88, p. 055101, 2017.
- [12] J. Yu, N. Koshikawa, Y. Arai, S. Yoda, and H. Saitou, "Containerless solidification of oxide material using an electrostatic levitation furnace in microgravity," *Journal of crystal growth*, vol. 231, pp. 568-576, 2001.
- [13] P.-F. Paradis, T. Ishikawa, and S. Yoda, "Non-contact measurements of surface tension and viscosity of niobium, zirconium, and titanium using an electrostatic levitation furnace," *International journal of thermophysics*, vol. 23, pp. 825-842, 2002.
- [14] Y. Sung, H. Takeya, K. Hirata, and K. Togano, "Spherical Nb single crystals containerlessly grown by electrostatic levitation," *Applied physics letters*, vol. 82, pp. 3638-3640, 2003.

- [15] G. Lohoefer and I. Egry, "Measuring thermophysical properties of undercooled liquid metals in microgravity," 1992.
- [16] A. B. Hanlon, D. M. Matson, and R. W. Hyers, "Microgravity Experiments on the Effect of Internal Flow on Solidification of Fe-Cr-Ni Stainless Steels," *Annals of the New York Academy of Sciences*, vol. 1077, pp. 33-48, 2006.
- [17] C.-H. Chun, "Marangoni convection in a floating zone under reduced gravity," *Journal of crystal growth*, vol. 48, pp. 600-610, 1980.
- [18] S. Lu, H. Fujii, and K. Nogi, "Marangoni convection and weld shape variations in Ar-O₂ and Ar-CO₂ shielded GTA welding," *Materials science and engineering: A*, vol. 380, pp. 290-297, 2004.
- [19] J. Lee, S. Liu, and R. Trivedi, "The effect of fluid flow on eutectic growth," *Metallurgical and Materials Transactions A*, vol. 36, pp. 3111-3125, 2005.
- [20] D. Matson, "Growth competition during double recalescence in Fe-Cr-Ni alloys," *MRS Online Proceedings Library Archive*, vol. 551, 1998.
- [21] W. A. Tiller, K. A. Jackson, J. W. Rutter, and B. Chalmers, "The redistribution of solute atoms during the solidification of metals," *Acta Metallurgica*, vol. 1, pp. 428-437, 1953/07/01/ 1953.
- [22] R. Hermann, W. Löser, G. Lindenkreuz, A. Diefenbach, W. Zahnnow, W. Dreier, *et al.*, "Metastable phase formation in undercooled Fe-Co melts," *Materials Science and Engineering: A*, vol. 375, pp. 507-511, 2004.
- [23] M. Li, X. Lin, G. Song, G. Yang, and Y. Zhou, "Microstructure evolution and metastable phase formation in undercooled Fe-30 at.% Co melt," *Materials Science and Engineering: A*, vol. 268, pp. 90-96, 1999.
- [24] D. M. Herlach, "Non-equilibrium solidification of undercooled metallic metls," *Materials Science and Engineering: R: Reports*, vol. 12, pp. 177-272, 1994/08/01/ 1994.
- [25] Y. Wu, J. Chang, W. Wang, and B. Wei, "Metastable coupled-growth kinetics between primary and peritectic phases of undercooled hypoperitectic Fe₅₄. 5Ti₄₅. 5 alloy," *Applied Physics Letters*, vol. 109, p. 154101, 2016.
- [26] Y. K. Zhang, J. Gao, M. Kolbe, S. Klein, C. Yang, H. Yasuda, *et al.*, "Phase selection and microstructure formation in undercooled Co-61.8at.% Si melts under various containerless processing conditions," *Acta Materialia*, vol. 61, pp. 4861-4873, 2013/08/01/ 2013.
- [27] W. J. Yao, N. Wang, and B. Wei, "Containerless rapid solidification of highly undercooled Co-Si eutectic alloys," *Materials Science and Engineering: A*, vol. 344, pp. 10-19, 2003/03/15/ 2003.
- [28] J. E. Rodriguez, C. Kreisler, T. Volkmann, and D. M. Matson, "Solidification velocity of undercooled Fe-Co alloys," *Acta Materialia*, vol. 122, pp. 431-437, 2017/01/01/ 2017.
- [29] R. Hermann and W. Löser, "Growth kinetics of undercooled Fe-Co melts," *Journal of Magnetism and Magnetic Materials*, vol. 242-245, pp. 285-287, 2002/04/01/ 2002.
- [30] J. Lipton, W. Kurz, and R. Trivedi, "Rapid dendrite growth in undercooled alloys," *Acta Metallurgica*, vol. 35, pp. 957-964, 1987.

- [31] D. Matson, "The measurement of dendrite tip propagation velocity during growth into undercooled metallic melts," *Solidification 1998, Indianapolis, IN*, pp. 233-244, 1998.
- [32] O. Funke, G. Phanikumar, P. Galenko, L. Chernova, S. Reutzel, M. Kolbe, *et al.*, "Dendrite growth velocity in levitated undercooled nickel melts," *Journal of Crystal Growth*, vol. 297, pp. 211-222, 2006.
- [33] D. M. Herlach, "Dendrite growth kinetics in undercooled melts of intermetallic compounds," *Crystals*, vol. 5, pp. 355-375, 2015.
- [34] R. Trivedi, H. Franke, and R. Lacmann, "Effects of interface kinetics on the growth rate of dendrites," *Journal of Crystal Growth*, vol. 47, pp. 389-396, 1979.
- [35] M. Flemings, D. Matson, and J. Rogers, "Levitation observation of dendritic evolution in steel ternary alloy rapid solidification (LODESTARS)," *NASA Science requirements document*, 2003.
- [36] T. Aoyama, Y. Takamura, and K. Kuribayashi, "Dendrite growth processes of silicon and germanium from highly undercooled melts," *Metallurgical and Materials Transactions A*, vol. 30, pp. 1333-1339, 1999.
- [37] D. Bouchard and J. S. Kirkaldy, "Prediction of dendrite arm spacings in unsteady-and steady-state heat flow of unidirectionally solidified binary alloys," *Metallurgical and Materials Transactions B*, vol. 28, pp. 651-663, 1997.
- [38] N. Bergeon, F. L. Mota, L. Chen, D. Tournet, J. Debierre, R. Guérin, *et al.*, "Dynamical microstructure formation in 3D directional solidification of transparent model alloys: in situ characterization in DECLIC Directional Solidification Insert under diffusion transport in microgravity," in *IOP Conference Series: Materials Science and Engineering*, 2015, p. 012077.
- [39] N. Bergeon, D. Tournet, L. Chen, J.-M. Debierre, R. Guérin, A. Ramirez, *et al.*, "Spatiotemporal dynamics of oscillatory cellular patterns in three-dimensional directional solidification," *Physical review letters*, vol. 110, p. 226102, 2013.
- [40] H. N. Thi, Y. Dabo, B. Drevet, M. Dupouy, D. Camel, B. Billia, *et al.*, "Directional solidification of Al-1.5 wt% Ni alloys under diffusion transport in space and fluid-flow localisation on earth," *Journal of crystal growth*, vol. 281, pp. 654-668, 2005.
- [41] Z. Jian, K. Kuribayashi, and W. Jie, "Solid-liquid interface energy of metals at melting point and undercooled state," *Materials Transactions*, vol. 43, pp. 721-726, 2002.
- [42] G. W. Lee, S. Jeon, C. Park, and D.-H. Kang, "Crystal-liquid interfacial free energy and thermophysical properties of pure liquid Ti using electrostatic levitation: Hypercooling limit, specific heat, total hemispherical emissivity, density, and interfacial free energy," *The Journal of Chemical Thermodynamics*, vol. 63, pp. 1-6, 2013/08/01/ 2013.
- [43] A. F. Guillermet, "Critical evaluation of the thermodynamic properties of cobalt," *International Journal of Thermophysics*, vol. 8, pp. 481-510, 1987.
- [44] X. Han, N. Wang, and B. Wei, "Thermophysical properties of undercooled liquid cobalt," *Philosophical magazine letters*, vol. 82, pp. 451-459, 2002.

- [45] L. Zhang, Y. Du, H. Xu, and Z. Pan, "Experimental investigation and thermodynamic description of the Co–Si system," *Calphad*, vol. 30, pp. 470-481, 2006/12/01/ 2006.
- [46] M. Barth, B. Wei, and D. Herlach, "Crystal growth in undercooled melts of the intermetallic compounds FeSi and CoSi," *Physical Review B*, vol. 51, p. 3422, 1995.
- [47] N. Kang, P. Coddet, C. Chen, Y. Wang, H. Liao, and C. Coddet, "Microstructure and wear behavior of in-situ hypereutectic Al–high Si alloys produced by selective laser melting," *Materials & Design*, vol. 99, pp. 120-126, 2016/06/05/ 2016.
- [48] K. G. Prashanth and J. Eckert, "Formation of metastable cellular microstructures in selective laser melted alloys," *Journal of Alloys and Compounds*, vol. 707, pp. 27-34, 2017/06/15/ 2017.

Appendices

A	Procedure for Sample Making	9
B	ESL Experimental Procedure	10
C	Image processing script	11

A) Procedure for CoSi Sample Making

1. Calculate mass fraction of Cobalt and Silicon using Excel file.
2. Cut the material needed. I used pliers to cut 99.95% pure Cobalt rods into small fragments.
3. The cut fragments of Cobalt were then sanded to reach the desired mass, and 99.999% Silicon beads were only weighed to match the calculated mass within ± 0.03 mg. Tweezers, sand paper P220, sample trays, gloves, metal-specific filler were utilized to prevent contamination. A max of 2 pieces for each element were allowed per sample. This reduces possible fragment loss during the arc-melting process.
4. Samples are massed and sealed in test tubes.
5. Samples are shipped and arc-melted at the NASA MSFC in a Ar atmosphere. It is important that arc-melted samples are cooled quickly to reduce the amount of oxide absorption. To help, a large Zr sample is placed with the sample set. The cooling rate of the Zr sample is decreased due to its relatively large size allowing it to absorb the remaining oxygen molecules still within the arc-melting chamber.

B) ESL Experimental Procedure

1. Chamber of ESL is properly cleaned by NASA contractor.
2. ESL is sealed and inspected.
3. Water cooler and vacuum ($1E-11$ Torr # atm) are turned on.
4. A Zr sample is heated to absorb remaining oxides and to calibrate laser settings.
5. YAG laser position is set to center of levitated Zr sample using the Mikron Pyrometer. The peaks of the Time vs. Temp plot were indicators for the focal point of the pyrometer.
6. Samples are processed individually. A CoSi sample is loaded inside the entry port that leads to the plunger stem.
7. Raise the sample up into the testing region via sample holder (the "stem")
8. Turn laser on to heat sample to near melting temperature for desired amount of time to remove (at best) contaminants on surface that could potentially impact charging efficiency. Simultaneously vibrate system (shake sample) to prevent sample sticking onto holder.
9. Levitate sample and lower stem.
10. Melt and then superheat sample above the melting temperature.
11. Reduce heater control voltage to desired operating setting and hold heater control voltage until sample solidifies.
12. Turn off laser and cool to ambient, turn off levitation field and allow sample to drop for recovery.
13. The sample and temperature profile are carefully monitored for recalescence.
14. Retrieve sample and record mass. Save for image processing.
15. After the melt cycle, the pyrometer, laser power level, pressure are saved as (.xls) files for analysis.

C) Image processing Script

The following is the Vision Assistant script for a typical image analysis. Additional functions may be required due to the quality of the SEM machine.

1. Load SEM image
2. Mask information bar at bottom and confirm the new image size for scaling
3. Enhance image with changes in brightness, contrast, and gamma to better discern regional structures.
4. Convert photo to gray image (0-255 pixels).
5. Large images with variations can be sectioned into quadrants.
6. Perform Linear profile on primary structure to identify proper threshold values. This will convert the image to a binary image.
7. Smoothen edges images with reasonable equal values of dilation/erosion.
8. Use Particle filter to remove tiny pixels detected within the surrounding void (black contrast).
9. Use Advanced morphology to “fill in holes” within the grains. This is to account for % area coverage.
10. Circle detection will identify the structures and can supply a excel file with all identified circles with corresponding radii in pixels.
11. Possible to have multiple circles detected within the same dendrite structure and must be removed from calculation.
12. Particle analysis can be used to detect the total active pixels in the binary image. This function can also provide an excel file with identified structures and corresponding area in pixels².